PERFORMANCE AND TRADE-OFFS OF AN AMPLITUDE-STEERED ARRAY

BY

VIRGINIE LASSALE

Dipl. Grad. Ingen., ENST, 2000

THESIS

Submitted in partial fulfillment of the requirements
for the degree of Master of Science in Electrical Engineering
in the Graduate College of the
University of Illinois at Urbana-Champaign, 2001

Urbana, Illinois

UNIVERSITY OF ILLINOIS AT URBANA-CHAMPAIGN

GRADUATE COLLEGE

December, 2001
date

WE HEREBY RECOMMEND THAT THE THESIS BY

Virginie Lassale

ENTITLED _____ Performance and Trade-Offs

of an Amplitude-Steered Array

BE ACCEPTED IN PARTIAL FULFILLMENT OF THE REQUIREMENTS FOR

THE DEGREE OF _____ Master of Science

Director of Thesis Research

Head of Department

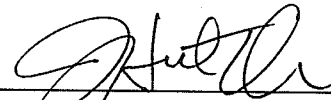Committee on Final Examination†

Chairperson

†Required for doctor's degree but not for master's.

O-517

UNIVERSITY OF ILLINOIS AT URBANA-CHAMPAIGN

GRADUATE COLLEGE DEPARTMENTAL FORMAT APPROVAL

THIS IS TO CERTIFY THAT THE FORMAT AND QUALITY OF PRESENTATION OF THE THESIS SUBMITTED BY <u>VIRGINIE LASSALE</u> AS ONE OF THE REQUIREMENTS FOR THE DEGREE OF <u>MASTER OF SCIENCE</u> ARE ACCEPTABLE TO THE DEPARTMENT OF ELECTRICAL AND COMPUTER ENGINEERING.

<u>DECEMBER 5, 2001</u>
Date of Approval

_____
Departmental Representative

DEDICATION

To my family and my friends

ACKNOWLEDGMENTS

TABLE OF CONTENTS

vi

LIST OF TABLES

LIST OF FIGURES

Figure

ix

CHAPTER 1

INTRODUCTION

In *American Genesis*, Thomas Hughes suggests that the convergence of two technologies can cause a revolution [1989]. This is precisely what happened when X-rays met computers and produced ultrasound imaging. X-rays were discovered in Germany at the end of the nineteenth century and the first computers appeared in the 1940s. These technologies benefited from the advances of World War II, and in particular from the improvement of the sonar technology. In 1945, newly demobilized American, British, German, and Japanese experts in submarine warfare thought to adapt ultrasound to medical diagnosis [*Kevles*, 1997]. In 1946, William Fry founded the University of Illinois Bioacoustics Laboratory and designed a sophisticated way of focusing high-frequency sound waves. In the meantime, by 1950, the MIT Laboratory built an ultrasonic brain scanner. In the 1970s, gray-scale ultrasound was developed and ultrasound imaging became an accepted diagnostic tool. Because these techniques are noninvasive and nondestructive, they have been applied in many fields: medical imaging, subsurface imaging, or nondestructive evaluation. In medicine, this technology has grown in utility and is used routinely in diagnosis. The current knowledge suggests that diagnostic ultrasound ranks along with the stethoscope as one of the safest tools used in medicine. The images are produced via ultrasound energy scattered from the tissue's boundaries and smaller structures within the tissues. Ultrasound is extensively used in obstetrics and gynecology, in particular to assess fetal health or detect cancer. Indeed, ultrasound can distinguish between innocent liquid-filled cysts and solid tissue that requires a biopsy. In addition, ultrasound is being developed to image the heart [*Kanai*, 1993] or the abdominal organs, and to characterize the ocular tissue [*Ye et al.*, 1995] or the skin [*Passmann and Ermert*, 1996]. It can been used in dentistry also because ultrasonic waves are particularly sensitive to tight cracks and fine interface layouts, often difficult to interpret in dental x-ray images. With the advent of Doppler techniques, ultrasound has become a

valuable diagnostic tool to measure the speed of blood and detect abnormalities [*Jensen*, 1996a]. Currently, hyperthermia is a technique developed to treat cancers [*Fujii*, 1999]

From its inception about 30 years ago, a lot of research has been done to improve the resolution of the images, the efficiency of the transducers, and the processing of the data. The efficiency of these techniques increased and their cost was reduced. Currently, piezoelectric transducers are usually used to collect the data. The ultrasonic system can be operated with different methods: pulse-echo mode, transmission methods, and Doppler methods. In the pulsed-echo mode, a single probe is used for both transmitting the signal and receiving the echoes reflected or scattered back from the tissues. Usually, this method is used for diagnostic imaging and the transducers are often an array of elements. In transmission methods, two transducers are used and the ultrasonic attenuation along the path is measured. Finally, the Doppler effect can be used to detect tissue or organ movement, or blood flow in vessels.

In this thesis, an amplitude-steered array is studied, and the pulse-echo method is used. Therefore, this method will be the only one presented in the introduction, and two conventional techniques, amplitude mode (A-Mode) and brightness mode (B-Mode), will be explained. They represent the basis of the further development, and their study is necessary for a good understanding of the amplitude-steered array. The remainder of the introduction gives some background information concerning real-time imaging. A brief study of mechanically steered transducers is followed by the overview of electronically steered arrays. It will be shown that these techniques make real-time imaging possible, but their frame rate is limited. In this study, the properties of an amplitude-steered array will be studied to determine if it can produce medical images at a higher rate. The number of images formed per second is important, particularly in cardiology. Finally, the organization of this thesis is given in the last part of the introduction.

1.1. Pulse-Echo Systems

Currently, the following are the most utilized systems in diagnostic imaging, especially for echography [*LaFollette and Ziskin*, 1986] or cardiography [*Kanai H. et al.*, 1993].

1.1.1. Amplitude mode

The earliest instruments used this technique, and it is the simplest one. The instrument sends a signal and then measures the echo amplitude. A display of the amplitude as a function of depth of penetration (or A mode display) is obtained. The depth of penetration is computed as $ct/2$, where c is the speed of sound in the tissue and t is the time of flight of the pulse. A pulse generator transmits a high-voltage pulse train to the transducer. The peak-to-peak voltage is more than 100 V and the pulse repetition frequency, PRF, is approximately 1 kHz. In this type of system, PRF and depth of penetration are related since the transducer should wait to receive all the echoes from structures of interest before it transmits another pulse. According to the values of attenuation, power levels, and resolution we want to achieve, different PRF can be chosen. The center frequency of the pulse is chosen between 1 MHz and 15 MHz, depending of the depth of the organs to image. Historically, for abdominal, brain, and cardiac imaging, the frequencies ranged from 2 to 5 MHz. Higher frequencies (5 to 15 MHz) are used in ophthalmology or in peripheral blood vessel studies.

The backscattered ultrasound pressure wave that returns to the transducer produces a voltage proportional to the strength of the wave. The dynamic range of the echo amplitude can be 70 or 80 dB, thus the signal is logarithmically compressed before it is amplified. Since the attenuation of the wave in the tissue must be taken into account, the gain of the amplifier is increased with time to compensate for the loss of energy in the tissues. Finally, digitalization and envelop detection finish the processing of the signal.

1.1.2. Static brightness mode

In the brightness mode, the echo amplitude modulates the electron beam intensity of a cathode ray tube, and a gray-scale B-mode display is obtained. Two-dimensional images are formed in using several A lines. For each A line, the received signal is amplified with preamplifier and time-variable gain amplifier, then logarithmically compressed and filtered to remove the carrier signal. This type of scanner is called static B-scanner in contrast to real-time B-scanner because the time to form one image is several minutes. Therefore, for the study of structures in motion such as the heart, the real-time method must be used. In addition, manual B-scan systems depend on operator skill and are time consuming.

1.2. Real-Time Methods

Several methods are currently used to achieve the formation of images fast enough so that the motion of an organ can be displayed. The beam is mechanically or electronically steered, thus the scanning technique does not depend as much on the operator skills. First, several concepts will be defined because they will be useful to compare the different techniques. Second, the performances of these methods are compared and their advantages or drawbacks are studied.

1.2.1. Useful definitions

- Lateral resolution and focusing:

If the transducer produced an infinitely narrow beam, the polar coordinates of a reflector could be determined exactly from the direction of the beam and the time until the reflection was received. The lateral resolution is the ability to distinguish two points close together at the same depth, and it can be defined primarily as the width of the beam. If the beam width of a transducer is smaller than the distance between two objects, the system can separate them. Otherwise, they cannot be distinguished in the image. The concept of lateral resolution is presented in more detail in Chapter 2. Because a transducer may have a diameter of 1 to 5 cm, the lateral resolution is very poor if some form of beam focusing is not used. Focusing the beam results in a reduction of the beam width, and thus it improves the lateral resolution. The on-axis depth-of-focus (DOF) is defined as the distance over which a point reflector produces an echo reduced in amplitude by 50% from that at the focal point.

- Axial resolution:

The axial resolution is the ability to distinguish between two scatterers at the same lateral position and close in range. Ideally, the exciting pulse would have an infinitesimal time duration and an infinite bandwidth. This ideal is impossible to achieve, but the best axial resolution is achieved by the shortest pulses with broad frequency support. This will be explained in detail in Chapter 2.

- Frame rate and depth of field:

Currently, most ultrasonic systems allow for the propagation of one pulse at a time in the field of interest and each pulse forms only one line in the image. This puts a constraint on real-

4

time scanners because the maximum frame rate R_f, the depth of field D, the number of scan lines N, and the speed of sound c are related by

$$R_f.D.N = c/2 \qquad (1.1)$$

There is a trade-off between frame rate, depth of field, and the number of lines. To have a high frame rate and a correct display of the motion, the depth of field or the lateral resolution must be reduced. For large organs, such as the liver, the field of view should be deep and broad in the meantime. Therefore, if the DOF is large enough to represent the entire organ, the number of lines is reduced and the quality of the images is poor. Thus, high-quality images of large organs are difficult to obtain. Typically, there are 128 lines in a real-time ultrasonic image. If the frame rate is 30 frames/s, the penetration cannot be deeper than 19.5 cm.

1.2.2. Different methods for real-time imaging

- Mechanically steered scanners:

Mechanical scanners are moved laterally or rotated. A dome of plastic houses the transducer and it is bathed in a fluid. The system is moved back and forth on the skin of the patient. For each movement, an image is formed. To obtain a narrow beam at the depth of interest, a focused transducer can be used. For this purpose, a concave lens can be placed in front of the transducer or the transducer itself can be manufactured in a curved form. The curvature of the transducer is characterized by the f-number, by analogy to an optical lens used for photography. The f-number is given by

$$n_f = R/(2a), \qquad (1.2)$$

where R is the radius of curvature of the lens and a is the radius of the transducer. The focal distance F is related to R by

$$F \approx \frac{R}{1-\dfrac{1}{n_f}}. \qquad (1.3)$$

Using a lens to focus is useful because lenses with different focal distances can be chosen according to the type of application. Focusing improves the lateral resolution, and it also concentrates the energy of the ultrasound wave into a small region; thus, the waves reflected by objects at the focus with have a large amplitude and the image will have a higher SNR in that region.

Mechanical scanners have the advantage that they do not have grating lobe problems and they are not electronically complicated, as opposed to linear arrays. However, the focusing is realized with a lens and the lateral resolution outside the region of focus is poor, as opposed to electronically steered arrays. The second drawback of mechanically steered transducers is that the oscillation of the scanner on the skin may move the tissues and the images may be blurred.

- Sequential linear arrays:

Almost all commercial imaging transducers consist of an array of small piezoelectric crystals because they can steer the beam or change the position of the focal point easily. Three types of transducers can be used: linear arrays with synthetic aperture, linear phased array, and annular arrays. Linear arrays are composed of piezoelectric elements sequentially excited by a pulse generator. Usually, the transducer is composed of 64 to 512 rectangularly shaped elements. The elements are not focused and they are isolated from their neighbors. A voltage pulse is sent to a group of elements, as illustrated in Figure 1.1. (All figures and tables appear at the end of the chapter.) Here, the group is composed of the first three elements of the array. The backscattered echo is received and the next group of elements (here, elements 2, 3, and 4) is excited. The beam is translated with respect to the first line. Another line is formed. Then, the process is repeated until all the elements have been excited. The image formed has a rectangular field of view and each column corresponds to an excitation of three elements. Thus, the width of the image obtained depends on the width of the transducer.

In the previous example, one line was formed by elements 1, 2, and 3; another by elements 2, 3, and 4; and another by elements 3, 4, and 5. Therefore, the excitation of five elements yields the formation of three lines. More generally, this type of array allows one to form almost twice as many scan lines as there are elements. It is usually used when a large field of view is required. These arrays are usually 1 cm wide and 10 to 15 cm long.

However, linear sequenced arrays are essentially unfocused devices, and focusing must be introduced by designing a curved array or adding a cylindrical lens to the array. For applications where there is only a limited window such as cardiac examinations, focused arrays with smaller apertures, as linear phased arrays, are preferred. In addition, the quality of the image may be degraded by the presence of side lobes. The problem raised by the side lobes will be discussed in more detail in Chapter 2.

- <u>Linear arrays with synthetic aperture:</u>

With this method, the elements of the array are excited one at a time, sequentially. All the signals reflected are stored and then processed. After synthetic aperture processing, an A-line is the sum of the received signals from the different elements. If the signals are delayed appropriately, the beam can be focused at a particular point. Figure 1.2 represents an array of five elements and P is the focus point. To have a focused beam in P, the signals from the different elements must be coherent. Because the array is linear, the distance between the elements and the focus varies throughout the aperture. Thus, the signals from the elements with the shorter path lengths must be delayed appropriately. For example, in Figure 1.2, the signal corresponding to the last element of the array reaches the point P after the signal coming from the center of the array. The difference in the time of flight is 2τ. If we want to have coherent signals, the signal received by the element in the center of the array must be delayed by a time 2τ. The delayed signals are added and processed. The best focusing is obtained with large aperture and a large number of elements. In addition, the elements should have a large beam spread and thus a small size, and their spacing should be small enough to avoid grating lobes.

Synthetic apertures produce images of good quality in the region of focus and they are electronically simple. In addition, the beam can be focused at multiple depths with an appropriate processing, which is impossible for fixed focused transducers.

However, the images suffer of a large SNR because only one element is excited at a time.

- <u>Linear phased arrays:</u>

There are two differences between sequential arrays and linear phased arrays. First, all the elements of the phased array are excited for each line formed in the image, rather than a subset as in sequential arrays. Second, the voltage pulses exciting the elements are delayed in time so that the beam is focused and steered.

As illustrated in Figure 1.3, focusing can be achieved and the principle is the same as for synthetic aperture. But for arrays with synthetic aperture, the elements are excited successively, i.e., only one element emits a signal for each exciting pulse. The received signals are then delayed and processed. In the phased arrays, for each exciting pulse, all the elements emit a signal. However, the emitted signals are delayed to focus the beam.

With this method, the images are high quality because the beam can be focused at many depths and the SNR is high. With B-mode imaging, the depth of focus is limited and synthetic apertures have a low SNR because the individual elements are excited in sequence and they do not have a high power.

However, linear phased arrays are electronically complicated in comparison to the previous techniques. In addition, they require complex data collection and processing. Indeed, several pulses must excite the elements to obtain a single A line because the focusing is made at several depths. Finally, if the elements are not close enough, grating lobes can be formed and degrade the image quality.

- Annular arrays:

Annular arrays are made by an alternation of concentric circular piezoelectric elements and isolated material. It is possible to use appropriate delay lines to achieve focusing, but the beam cannot be steered. The focus point has to be on the axis of the annular array. Thus, the transducer must be moved mechanically to form an image.

To sum up, the current transducers allow either the steering or the focusing of the beam, or both. However, the most powerful techniques are also the more electronically difficult to implement. In addition, according to Equation (1.1), none of these techniques can achieve a frame rate greater than 30 images per second for a depth of field of 20 cm and a number of 128 lines in the image. However, some examinations, for example in cardiology, require a higher frame rate. Each cardiac cycle is composed by two phases, the diastole and the systole. During the diastole, the atroventicular valves open and the blood fills the ventricles. During the systole, the blood is ejected from the ventricle in the aorta artery. Systole can be subdivided in a short phase called "rapid ejection" and a longer phase called the "reduced ejection." Systole lasts only 0.4 s and the rapid ejection 0.1 s. If the frame rate of the system used to image the heart is 30 frames per second, only three images will be formed during the rapid ejection. The information collected is insufficient to diagnose heart failure, in particular if the heart is hypodynamic or dilated [*Berne*, 1998].

1.3. Amplitude-Steered Array

1.3.1. Pennsylvania State University, 1976

In 1976, *Hughes and Thomson* proved that, by appropriately processing the output signals of the elements of a linear array, a tilted beam pattern can be produced without numerous delay lines or phase-shift network [1976]. The system they propose is interesting for underwater acoustics, particularly when the position of source or receiver is fixed. In that case, it is desirable to steer the direction of maximum response of the sum pattern of the source or receiver array to bearing angles other than straight ahead. In the array of study, only one ±90° phase shift is required and the steering angle can be varied in modifying the amplitudes of the outputs of the individual elements. This technique is called amplitude-weighting and it will be explained in detail in Chapter 2. In this article, the experimental results are obtained with a 9-elements array with a 0.5 wavelength spacing [*Hughes*, 1975]. The pattern is tilted as much as 30° from the array normal without the side lobe levels to exceed –30 dB. In the experiments presented, the beam is steered to a particular direction at a particular frequency and the study focuses on the level of the side lobes. The fact that the angle of tilt changes with frequency is considered a drawback of the system.

1.3.2. University of Illinois, 2000

Almost 25 years later, *Frazier et al.* use the change in steering direction with frequency to design a fast imaging system [2000a]. In that article, a new system called amplitude-steered array is studied. The maximum array response is swept over a range of angles by exciting the array with a frequency modulated chirp signal. For each pulse, a sector is scanned leading to fast two-dimensional imaging, compared to conventional imaging that uses one transmit pulse for each steering direction. This study focuses on the determination of the axial and lateral resolution, and their variation with the size of the array. The axial and lateral resolution are first computed and then measured with arrays of 300 to 700 elements. These concepts and the functioning of this array will be explained in more detail in Chapter 2. This device is very interesting because it can be used to perform three-dimensional imaging. In her Ph.D. dissertation [2000b], *Frazier* studies a system composed of an amplitude array and a synthetic aperture in the azimuthal direction. This system allows one to quickly obtain two-dimensional

images for a particular height z. In regrouping these 2D-images, a three-dimensional image can be formed. This work concerned mostly underwater acoustics and no attenuation was taken into account in the medium of propagation.

1.4. Organization of this Thesis

The following work discusses the variation of the performance of an amplitude-steered array. In Chapter 2, the theoretical development explains how this array forms 2-D real-time images, defines the axial and lateral resolutions, and describes the methodology used in the simulations. In Chapter 3, experimental results are presented: they show the variation of the resolutions with the length of the array, the focal distance, and the attenuation. The use of several arrays to broaden the field of view is studied at the end of this chapter. Finally, the conclusions of this work and the suggestions for future work are presented in Chapter 4.

Line 1   **Line 2**   **Line 3**

1 2 3 4 5 6 7 8 9 10 11 12   1 2 3 4 5 6 7 8 9 10 11 12   1 2 3 4 5 6 7 8 9 10 11 12
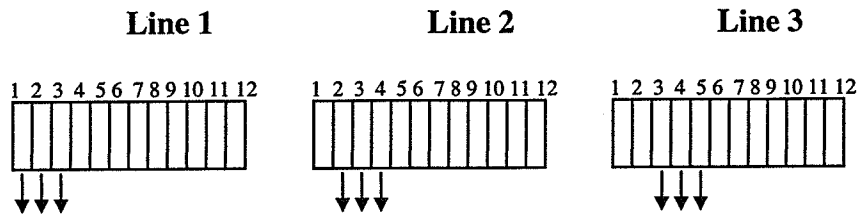
Figure 1.1 Linear sequenced array.
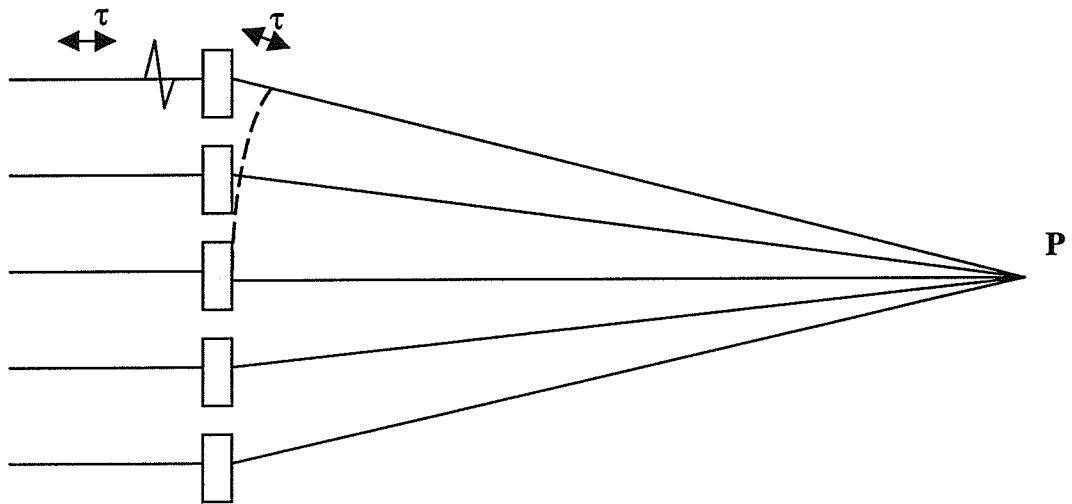
Figure 1.2 Focusing of the beam with a linear array using synthetic aperture processing.
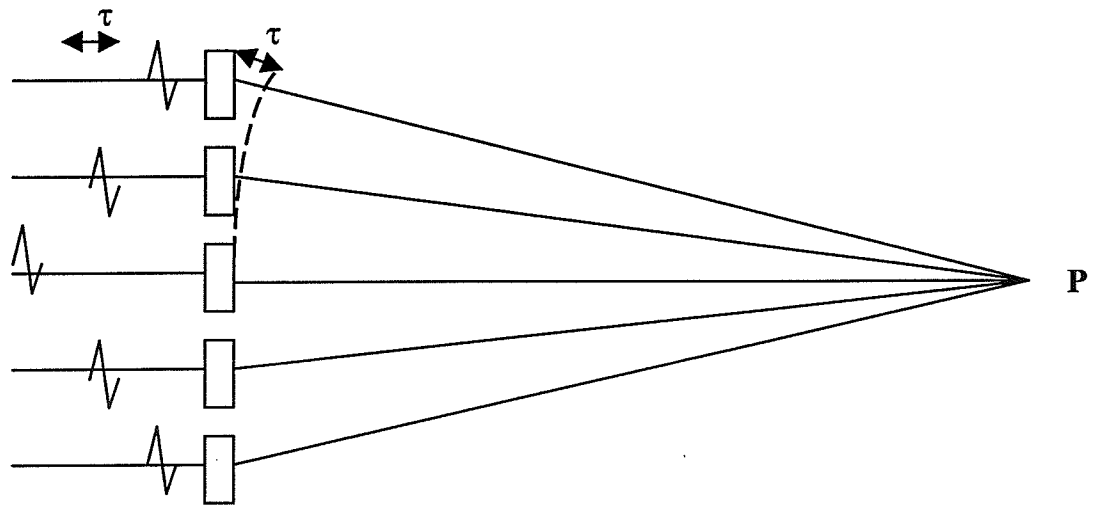
Figure 1.3 Focusing of the beam of a linear phased array by appropriately delaying excitation pulses to different elements.

CHAPTER 2

METHODOLOGY

2.1. Beam Steering

2.1.1. Field pattern for a linear phased array

In the following work, the system being studied is a linear array of equally spaced, equiamplitude point sources. To understand how the beam is steered by amplitude weighting the elements of this array, we will first determine the field pattern of a plain linear phased array. If we excite all the sources of a phased array simultaneously with the same signal of frequency ω, then the far-field pressure can be expressed as

$$P(r,\theta) = \frac{e^{-jkr}}{r} \sum_n e^{jnd\sin\theta} = \frac{Ne^{-jkr}}{r} H(\theta), \qquad (2.1)$$

where N is the number of elements of the array, k is the wave number at the frequency ω, d is the center-to-center spacing between the elements, θ is the angle measured from the array broadside direction, and r is the range of the point considered. Figure 2.1 represents the geometry of the system and the notations used.

The field pattern of the array, $H(\theta)$, can be expressed as

$$H(\theta) = \left| \frac{1}{N} \frac{\sin\left(\dfrac{N}{2}kd\sin\theta\right)}{\sin\left(\dfrac{1}{2}kd\sin\theta\right)} \right|. \qquad (2.2)$$

A plot of the beam pattern for a line array of in-phase elements radiating sound of wave number k with kd = 8 and N = 5 is plotted in Figure 2.2.

According to Equation (2.2), the denominator may vanish for $(1/2)\,kd|\sin\theta| = m\pi$, if m is an integer, but the numerator vanishes also. Thus we have a major lobe at $\theta = 0°$ and additional major lobes, called grating lobes, at θ such that

$$|\sin\theta| = \frac{m\lambda}{d}. \tag{2.3}$$

The amplitude of a grating lobe is the same as the amplitude of the major lobe. Thus, the field pattern is maximum in several directions. Ideally, the received rf echo is the sum of all the reflections from targets with the direction of the main lobe. If grating lobes are present, the total reflection also includes contributions from targets illuminated by these lobes. Thus, targets with different lateral position will contribute to the signal corresponding to the major lobe. This yields an image with a smaller dynamic range, especially if the targets have a low contrast. This may also result in the formation of "ghost images" or copies of a target that appears at several positions in the image. To avoid these additional maxima, the aperture must be adequately sampled. If the value of λ/d is greater than 1, $m\lambda/d$ is greater than 1 also and no grating lobe appear. In the following simulations, the frequency typically ranges between 1.2 MHz and 5.6 MHz, and the speed of sound c is 1500 m/s. The wavelength λ is between 0.26 mm and 1.25 mm. The distance between the elements is 0.126 mm, so the ratio λ/d varies between 2.1 and 9.9. Therefore, this ratio is always greater than 1 and, when the beam is not steered, there is only one major lobe at $\theta = 0°$, and several side lobes which could be reduced by apodization. However, the improvement of image quality by lowering the sidelobe levels will not be studied in this work.

2.1.2. Beam steering for a linear phased array

The main advantage of a phased array is that it gives the possibility to transmit or receive in various directions without physically rotating the array. This can be accomplished by electronic steering: if a time delay $n\tau$ is inserted into the electronic signal for the nth element of the array, then the field pressure for this element is

$$P_n(r) = \frac{A}{r_n} e^{j[\omega(t+n\tau)-kr_n]}, \tag{2.4}$$

and the directional factor becomes

$$H(\theta) = \left| \frac{1}{N} \frac{\sin\left[\dfrac{N}{2}kd\sin\theta - \dfrac{c\tau}{d}\right]}{\sin\left[\dfrac{1}{2}kd\sin\theta - \dfrac{c\tau}{d}\right]} \right| = \left| \frac{1}{N} \frac{\sin\left[\dfrac{N}{2}kd(\sin\theta - \sin\theta_0)\right]}{\sin\left[\dfrac{1}{2}kd(\sin\theta - \sin\theta_0)\right]} \right|. \qquad (2.5)$$

The major lobe now points in the direction θ_0 given by $\sin\theta_0$ = cτ/d. Thus, the introduction of a progressive time delay steers the major lobe from θ = 0° to θ = θ_0. The geometry of the array is represented in Figure 2.3.

When the major lobe of the beam is steered at an angle θ_0, grating lobes can develop, even if they were not present when the beam was not steered. Indeed, according to Equation (2.5), the denominator vanishes for (½)kd(sinθ-sinθ_0) = mπ, that is, for sinθ = mλ/d-sinθ_0. Since *sinθ_0* ranges between –1 and 1, the only way to avoid grating lobes is to design the array such that the relation sinθ = mλ/d-1 cannot be satisfied. The values of *mλ/d-1* must therefore be greater than 1 for all integer *m*, and in particular for m = 1. Thus, *λ/d* must be at least greater than 2 to avoid grating lobes when the beam is steered. Since the values of *λ/d* used in the following work range between 2 and 10, grating lobes cannot develop.

2.1.3. Amplitude weighting

An alternative technique, amplitude weighting, steers the beam without using phase shifting. Let us rewrite the directional factor of a linear phased array with steering angle θ_0. In the frequency domain, the time-shift τ corresponds to a multiplication of the signal of the *n*th source by the factor $e^{-j(nk_0 d\sin\theta_0)}$, with sin$\theta_0$ = cτ/d and k_0 as the wave number at a particular frequency. The field directional factor of the array can be rewritten as

$$H(\theta) = \frac{1}{N}\sum_n e^{jnd(k\sin\theta - k_0\sin\theta_0)}. \qquad (2.6)$$

To simplify the expression, let u = (kd/2)sinθ and Φ = (k_0d/2)sinθ_0:

$$H(\theta) = \frac{1}{N}\sum_{-\frac{N}{2}+1}^{\frac{N}{2}} e^{j(2n-1)(u-\phi)}. \qquad (2.7)$$

In Equation (2.7), each negative exponential can be combined with a corresponding positive exponential:

$$H(\theta) = \frac{1}{N}\left[\sum_{n=0}^{N/2}\left(e^{j(2n-1)(u-\phi)} + e^{-j(2n-1)(u-\phi)}\right)\right].\qquad(2.8)$$

Then, we can use Euler's formula and *H(θ)* becomes

$$H(\theta) = \frac{2}{N}\left[\cos(u-\phi) + \cos(3(u-\phi))+...+\cos((N-1)(u-\phi))\right].\qquad(2.9)$$

Let us use the trigonometric identity cos(A-B) = cos(A)cos(B) + sin(A)sin(B) :

$$H(\theta) = (2/N)[\cos\Phi\cos u+\cos(3\Phi)\cos(3u)+...+\cos((N-1)\ \Phi)\cos((N-1)u)$$
$$+\sin\Phi\sin u+\sin(3\Phi)\sin(3u)+...\sin((N-1)\ \Phi)\sin((N-1)u)].\qquad(2.10)$$

This expression shows that the directional factor of a linear array whose major lobe is steered at $\theta = \theta_0$ by phase shifting can be interpreted differently. *H(θ)* could be the field pattern created by an array whose elements are weighted before the signal is applied. Indeed, in Equation (2.10), the terms *cos((2n-1)Φ)* and *sin((2n-1)Φ)* are constant so they can be interpreted as amplitude weights of the elements. This means that these terms do not vary when the frequency of the signal changes. The terms *cos((2n-1)u)* and *sin((2n-1)u)* can be interpreted as the field generated by pairs of elements on opposite sides of the center of the array, in phase or 180° out of phase, respectively.

Equation (2.10) thus corresponds to the sum of the outputs of two arrays:

• The phase symmetric array: This array combines elements on opposite sides of the center with equal amplitudes and in phase. It corresponds to the sum of the *cos((2n-1)u)* terms:

$$\left[e^{j(2n-1)u} + e^{-j(2n-1)u}\right] = \cos((2n-1)u).\qquad(2.11)$$

• The phase antisymmetric array: This array combines elements on the opposite side of the center of the array with equal amplitudes and 180° out of phase. It corresponds to the sum of the *sin((2n-1)u)* terms:

$$\left[e^{j(2n-1)u} + e^{j\pi}e^{-j(2n-1)u}\right] = \left[e^{j(2n-1)u} - e^{-j(2n-1)u}\right] = 2j\sin((2n-1)u).\qquad(2.12)$$

The *j* factor shows that the phase antisymmetric array is inherently 90° out of phase with the output of the phase symmetric array. To obtain the field pattern of Equation (2.6), the outputs of the two arrays must be added with a ±90° shift. If we add them with a +90° shift, the beam is

steered at $\theta = \theta_0$. Otherwise, it is steered at $\theta = -\theta_0$. The *cos((2n-1)Φ)* and *sin((2n-1)Φ)* factors are the amplitude weights that determine the steering angle.

This theoretical development is founded on the expression of the directional factor in the far field, given by Equation (2.2). The limit between the near field and the far field corresponding to the array is given by

$$r_{min} = L^2/4\lambda, \tag{2.13}$$

where L is the greatest extend of the source and λ the wavelength.

In the following work, the length of the array is usually 7.5 cm. The frequency we used is between 1.2 MHz and 5.6 MHz, so the wavelength is approximately 0.3 mm. For these values, $r_{min} = 4.6$ m. Thus, an object located beyond a distance of 4.6 m is in the far field, and closer is in the near field.

In the simulations, the beam steering is not obtained with two different arrays. The phase symmetric and phase antisymmetric arrays share the same space. A single aperture is defined. First, the elements in the aperture are weighted with the values *cos((2n-1)Φ)* and they are excited by a cosine signal:

$$s(t) = \cos\left(2\pi\left[f_{start} + \left(\frac{(f_{start} - f_{stop})}{2t_{total}}\right)t\right]t\right), \tag{2.14}$$

where f_{start} is the frequency at the beginning (t = 0) and f_{stop} is the frequency at the end (t = t_{total}) of the excitation signal. The reflected signal is received by the elements and stored. Then the elements are weigthed by the *sin((2n-1)Φ)* factors and the system is excited by a sine signal:

$$s(t) = \sin\left(2\pi\left[f_{start} + \left(\frac{(f_{start} - f_{stop})}{2t_{total}}\right)t\right]t\right). \tag{2.15}$$

The reflected signal is also received and stored. Finally, the two signals are combined. In the following , the resulting signal is called the "received signal."

2.1.4. Variation of the steering angle with frequency

In the amplitude-steered array described above, the beam is steered to an angle $\theta = \theta_0$ for a fixed frequency f_0 corresponding to the wave number k_0. Now, let us suppose that the frequency f is not fixed but varies with time. Let k_f be the wave number corresponding to the

frequency f: $k_f = 2\pi f/c$. The directional factor is the same as for Equation (2.5) except that k_f replaces f_0 and θ_f replaces θ_0:

$$H(\theta) = \left| \frac{1}{N} \frac{\sin\left(\dfrac{N}{2} k_f d(\sin\theta - \sin\theta_f)\right)}{\sin\left(\dfrac{1}{2} k_f d(\sin\theta - \sin\theta_f)\right)} \right|, \qquad (2.16)$$

where the subscript f shows that k and θ depend on f.

This pattern is obtained by applying the amplitude weights $cos((2n-1)\Phi)$ and $sin((2n-1)\Phi)$ to the elements. Since these weights are fixed at the beginning of the experiment, they do not change when the frequency varies, and we have

$$\phi = k_0 d \sin\theta_0 = k_f d \sin\theta_f. \qquad (2.17)$$

The new steering direction θ_f is given by

$$\theta_f = \sin^{-1}\left(\frac{f_0}{f} \sin\theta_0\right). \qquad (2.18)$$

In other words, if we apply certain amplitude weights to the elements and we increase the frequency of the signal, then the beam is steered to the axis of the array and the angle θ decreases. A plot of the variation of the steering angle with the frequency is shown in Figure 2.4 for an array designed to steer to 5° at 5.6 MHz.

2.2. Image Formation

We will use the amplitude-steered array in the pulse-echo mode. Each of the elements is both a transmitter and a receiver.

2.2.1. Transmitted and received signals

The signal used to excite the elements of the array is a linear FM chirp of finite duration. The elements are first excited by a cosine signal given by Equation (2.14). Then the system is excited by a sine signal given by Equation (2.15).

The duration of the signal is important in pulse-echo mode because the elements cannot transmit and receive in the same time, so the wave that comes back when the array is still emitting will not be taken into account. Thus the sector located directly in front of the system is not imaged. The depth of this field is given by $ct_{total}/2$, where c is the speed of sound. Typically,

we use a signal of t_{total} = 50 μs, such that the depth of this sector is only 3.75 cm. The frequency of the signal changes with time, from f_{start} = 1.2 MHz to f_{stop} = 5.6 MHz, so the beam sweeps a sector of 20° in 50 μs. The field of view is in the far field. The wave bounces off of the objects located in the sector insonified and is then received by the same array. Through processing the signal collected by the elements of the array, we can determine the polar coordinates of the objects, thereby localizing them. For example, let us suppose that we want to visualize a target at a range r of 2 m. During a time t_0, the array emits a signal and then it receives the echo from field. The wave that was reflected by the target will reach the array at a time t = t_0 + 2r/c, where c is the speed of sound in the medium. For a target at 2 m, the received signal last 2.6 ms. To find the position of the targets, we compute the short time Fourier transform (STFT) of the received signal using a window between 8 μs and 1 ms. Figure 2.5 (a) is a plot of the received signal. We first compute the FFT of the signal contained in the window at t = 0. Then, we compute the FFT of the signal in the window centered at a later time t_1. The same process is repeated until the entire signal has been processed. Usually, a 2^{11}-point fast Fourier transform (FFT) is used. In Figure 2.5 (a), the windows before and after translation are represented by the straight lines. The plot of the Fourier transform corresponding to the peak in the signal is represented in Figure 2.5 (b). The temporal position of the FFT window gives the range, and the frequencies contained within the window give the lateral position. For example, the signal contained in the first window corresponds to the wave reflected by the closest objects. More generally, let t_w be the time at the center of the temporal window. The signal received in that window corresponds to the wave reflected by a target located at a distance r from the array such that r = ct_w/2, where c is the speed of sound in the medium. Since the direction of the beam depends on the frequency of the signal, the frequencies in the received signal gives the information we need to find the lateral position. The frequency of the signal is related to the angular position θ_f by Equation (2.18), with f_0 as the design frequency and θ_0 as the design angle. The weights are set at the beginning of the experiment such that the beam is steered to θ_0 at the frequency f_0.

2.2.2. Formation of the 2D image

The image we create is the normalized spectrogram of the signal. The x-axis represents the angular position θ of the point, the y-axis is its range. Each row represents the Fourier transform of the signal contained in the temporal window corresponding to the range considered.

In each row, the intensity of the pixel represents the value of the Fourier transform at the frequency corresponding to the angle considered. We use a logarithmic scale to plot the spectrogram. The function we plot is actually normalized and plotted with a logarithmic scale. Figure 2.6 is an example of a spectrogram for four-point targets in a nonattenuating medium. The targets are located at 6°, 9°, 15°, and 22°. Each row of the image corresponds to a certain temporal window and thus represents the range of the targets. Each column corresponds to a particular frequency (in this example, the frequency varies from 1.2 MHz to 5.6 MHz), and represents the angle related to the frequency. Of course, we can plot the spectrogram in a Cartesian system to have a better visualization of reality. In Figure 2.7 the spectrogram of an arc of circle of radius 2 m is represented.

2.3. Simulations

2.3.1. The spatial impulse response

The operation of the linear amplitude steered array has been simulated using the Field II program, developed by *J. A. Jensen* [1996*b*]. This program uses the concept of the spatial impulse response as developed by *Tupholme* [1969] and *Stephanishen* [1981]. Their approach relies on linear system theory to find the ultrasound field for the pulsed wave case, allowing any excitation to be applied to the transducer. When the transducer is excited by a Dirac delta function, the response gives the ultrasound field at a specific point in space as a function of time. Then, for any kind of excitation, we can find the field by convoluting the spatial impulse response with the excitation function. Since the impulse response varies with the position relative to the transducer, it is called spatial impulse response.

Furthermore, by acoustic reciprocity, the spatial impulse response equals the received response for a spherical wave emitted by a point source. Thus, we find the total received response in pulse-echo mode by convoluting the transducer excitation function with the spatial impulse response of the emitting aperture, and then with the spatial impulse response of the receiving aperture. Then we take into account the electromechanical transfer function of the transducer to yield the received voltage trace.

Any excitation can be applied to the transducer because linear system theory is used.

2.3.2. Focusing and apodization

Focusing and apodization can be handled in Field II through timelines. The signal is divided in segments: [0, t1], [t1, t2], etc. For each temporal interval, we define a focal point. The arrival time from the field point to the physical transducer element is used for deciding which focus is used. We can also set the focusing to be dynamic, so that the focus is changed as a function of time and thereby depth.

All the time values for focusing are calculated relative to a point on the aperture; generally, this point is set to (0,0,0). In the following simulations, we set the focusing point at (0,0,r), where r is the range of the targets we want to visualize.

Apodization could be used to lower the sidelobes. However, it will not be realized in the following work.

2.3.3. Attenuation

Field II can simulate the field in an attenuating medium.

In the human body, the ultrasound wave looses energy when it propagates in the tissues because of several mechanisms. The most important are the absorption of energy via tissue relaxation and scattering of the beam. The combinaison of these mechanisms is called ultrasonic attenuation and it depends on the frequency of the wave.

- Absorption:

The absorption losses are due to the conversion of ultrasonic mechanical energy into heat. Two major mechanisms yield absorption losses. First, "classical absorption" occurs with the friction between particles as they are displaced by the passage of the ultrasound wave. This causes an exponential decrease with distance in the pressure of the wave:

$$p(z) = p_0 \exp(-\beta_{abs} z), \qquad (2.19)$$

where β_{abs} is the absorption coefficient, z the distance of propagation, p_0 the initial pressure and p the pressure at the distance z from the origin. Classical absorption has a frequency squared dependence. The second mechanism participating in the absorption losses is the called relaxation. If the molecules are displaced from their position by an ultrasonic wave, they need a time τ to return to their original position. This process is characterized by a relaxation absorption coefficient β_{rel} whose frequency dependence is given by

$$\beta_{rel} = \frac{f^2}{1 + \left(\dfrac{f - f_{max}}{f_{max}}\right)^2}, \qquad (2.20)$$

where $f_{max} = 1/\tau$ is the frequency at which the energy loss is maximum.

- Scattering:

When the beam encounters irregularities or particles that are smaller than the wavelength, the wave is scattered in random directions. The scattering process is characterized in terms of the scattering cross-section σ_s, defined as the power scattered by the particle per unit incident intensity. For scatterers very small in comparison to the wavelength λ, σ_s is proportional to $1/\lambda^4$. Thus, the effects of scattering are more important for higher frequencies.

- Attenuation:

Attenuation is the sum of scattering, reflection, refraction, and absorption of the wave in the tissues. It is characterized by an exponential decrease in intensity:

$$I(z) = I_0 exp(-2\beta_{att}z), \qquad (2.21)$$

where I_0 is the initial intensity, I is the intensity after a propagation of distance z, and β_{att} is the coefficient of attenuation in Neper/cm. The coefficient in decibel/cm is given by

$$\beta_{att}(dB/cm) = 8.686\beta_{att}(cm^{-1}). \qquad (2.22)$$

Even if the relationship with frequency for scattering and absorption is complex, there is a simple linear relationship between the coefficient of attenuation and the frequency. In the tissues, β_{att} has different values as measured in previous studies [*Porder*, 1987]. Bone and muscle have large attenuation coefficients of respectively 8.7 and 3.5 dB/cm/MHz. For fat, brain, liver, or kidney its value is only 0.6 to 0.9 dB/cm/MHz.

In Field II, frequency-dependent attenuation can be included in the simulation. The attenuation is included through a frequency-dependent term and a frequency-independent term. The frequency-dependent term is linearized through a center of frequency f_0, so that the attenuation is 0 dB at f_0. This is done to make the inclusion of the attenuation computationally efficient. Therefore, β_{att} has the expression

$$\beta_{att} \approx A(f-f_0) + B, \qquad (2.23)$$

where $A(f-f_0)$ is the frequency-dependent term and B is the frequency-independent term.

At a distance r_n from the nth element of the array, the amplitude of the field is attenuated by a factor $exp(-\beta_{att}r_n)$. A plot of the geometry of the array and the notations used is in Figure 2.8. If the distance r_n is much greater than the length of the array, we can write r_n as

$$r_n = r_{mean} - nd\sin\theta, \quad (2.24)$$

where d is the spacing between the elements and r_{mean} the distance from the center of the array. In using Equation (2.23), we have

$$exp(-\beta_{att}r_n) = exp[(A(f-f_0) + B)(r_{mean} - nd\sin\theta)]$$

$$= exp[A(f-f_0)r_{mean} - A(f-f_0)nd\sin\theta + Br_{mean} - Bnd\sin\theta].$$

If the length of the distance considered is far enough from the array, and if the frequency is close to the center of frequency f_0, the term $A(f-f_0)nd\sin\theta$ is much smaller than the other terms in the exponential and it can be neglected. Thus, the amplitude is attenuated by a factor

$$exp(-\beta r_n) \approx exp[Ar_{mean}(f-f_0) + B(r_{mean} - nd\sin\theta)]. \quad (2.25)$$

The term $Ar_{mean}(f-f_0)$ is frequency dependent and the term $B(r_{mean} - nd\sin\theta)f_0$ is frequency-independent. Therefore, in Field II, only the frequency-independent attenuation is varied over the aperture. Then the frequency-dependent attenuation is included in the response by using the mean distance to the aperture r_{mean}.

2.4. Performance of the System

2.4.1. Definition of the resolutions

The main goal of this work is to study of the properties of an amplitude-steered array in an attenuating medium. We will determine the variations in the performance of the array according to the following parameters: distance from the array, size of the array, with and without attenuation. Thus, we need to be able to quantify the performance of the array, i.e., the resolution of the images we obtain. Since its range and angular position determine the location of a target, we will use the axial and lateral resolution. Figure 2.3 is a diagram of the imaging geometry. The axial and lateral resolution are defined with reference to the steering direction. The axial direction is along the steering direction, the lateral direction is perpendicular to it. There are a number of measures which can be used to describe the spatial resolution of an imaging system: the three most common in the spatial domain are the point spread function

(PSF), the line spread function (LSF), and edge spread function (ESF). Since the PSF is the only definition used in this thesis, it will be the only method explained.

Let us suppose that a very small object is in the imaging field-of-view. The relationship between the image, I, and the object, O, can be represented by

$$I(x,y,z) = O(x,y,z)*h(x,y,z),$$ (2.26)

where '*' represents convolution and h is the three-dimensional PSF. To have an image exactly similar to the object, h should be a Dirac function in three dimensions. But in reality, the image is blurred compared to the object. Therefore, the PSF can be approximated by a Gaussian or a Lorentzian function. In one dimension, the resolution can be determined by using Rayleigh's criterion [*Kinsler et al.*, 2000]. If two point sources are separated by a distance greater than the full-width-at-half-maximum (FWHM), they can be resolved. This separation defines the spatial resolution in the dimension considered. Figure 2.9 illustrates this definition of the spatial resolution and the Rayleigh's criterion. If the PSF is expressed in dB, the spatial resolution corresponds to the −3 dB width of the PSF.

2.4.2. Theoretical determination of the lateral resolution

If the beams emitted by the array were infinitely narrow, then the field pattern of the array would be a line infinitely thin. However an amplitude-steered array, operated at the frequency *f*, has a directional factor given by Equation (2.16). For the angles θ close to θ_f, the term *sin[(½)kd(sinθ-sinθ_f)]* can be approximated by *(1/2)kd(sinθ-sinθ_f)*. So the directional factor becomes

$$H(\theta) = \frac{\sin\left[\dfrac{N}{2}kd(\sin\theta - \sin\theta_f)\right]}{\dfrac{N}{2}kd(\sin\theta - \sin\theta_f)}.$$ (2.27)

The lateral resolution is defined as the −3 dB of the pattern. The sinc function falls to −3 dB of its maximum value when its argument is equal to ±1.3894. Thus, to find the −3 dB angle, we must solve the equation

$$\frac{N}{2}kd\left(\sin\theta_{-3dB} - \sin\theta_f\right) = \pm 1.3894.$$ (2.28)

We obtain

24

$$\theta^{+}_{-3dB} = \sin^{-1}\left(\sin\theta_{r} + \frac{0.4423\lambda}{Nd}\right)$$ (2.29)

$$\theta^{-}_{-3dB} = \sin^{-1}\left(\sin\theta_{r} - \frac{0.4423\lambda}{Nd}\right)$$ (2.30)

and the lateral resolution in degrees is

$$\alpha = \theta^{+}_{-3dB} - \theta^{-}_{-3dB}.$$ (2.31)

2.4.3. Theoretical determination of the axial resolution

The axial resolution is defined as the closest separation of two reflectors, in the direction of the propagation, which results in echoes that can be resolved in time. The pulse length is given by

Pulse length(m) = pulse duration (s) x c (m/s), (2.32)

where c is the speed of sound in the medium and x is multiplication.

When the transducer is excited, the emitted pulse is not an infinitely short signal. The emitted signal has a duration t called the temporal length of the pulse. The time resolution in the pulse-echo mode depends on this parameter: the narrower the pulse, the better the time resolution. In traditional imaging, where the transducer is shock-excited, the spatial length is determined by the wavelength at the resonance frequency and the quality factor of the transducer Q. For this system, the axial resolution is defined as $\Delta r = Q\lambda/4$. Q represents the efficiency of the transducer. It is given by

$$Q = \frac{f_0}{\Delta f},$$ (2.33)

where f_0 is the resonance frequency and Δf is the –3 dB bandwidth of the impulse response.

In the amplitude-steered array, the system does not have a single resonance frequency. So we have to define a new parameter Q_{sig} such that

$$Q_{sig} = \frac{f}{\Delta f},$$ (2.34)

where f is the frequency of the received signal and Δf the bandwidth of the received signal, i.e., the range of frequency contained in the signal coming from the angle θ_r. We apply matched filtering to the received chirp for pulse compression. If the received signal had a single

frequency, the output of the matched filter would be a Dirac function. But in fact, the correlation between the received signal and the impulse response of the filter is a sinc function:

$$\rho = \frac{\sin\left(\dfrac{2\pi\Delta fr}{c}\right)}{\dfrac{2\pi\Delta fr}{c}} \quad , \tag{2.35}$$

where r is the range of the target corresponding to time t so that $r = ct/2$, and c is the speed of sound in the tissue. We use this correlation factor ρ to find the range of the target. The axial resolution Δr is determined by the -3 dB points of ρ.

The correlation factor ρ falls to -3 dB of its maximum value, when the argument of the sinc function is equal to ± 1.3894. Thus we have to solve the equation

$$\frac{2\pi\Delta fr_{-3dB}}{c} = 1.3894 . \tag{2.36}$$

The axial resolution is

$$\Delta r = 2r_{-3dB} = \frac{1.3894c}{\pi}\frac{1}{\Delta f} \tag{2.37}$$

But Δf depends on the center of frequency of the received signal, and we can express the axial resolution in terms of Q_{sig}:

$$\Delta r = 1.3894\frac{c}{\pi f}\frac{f}{\Delta f} = 0.4423Q_{sig}\lambda , \tag{2.38}$$

where λ is the wavelength of the signal.

To compute the axial resolution theoretically, we determine first the parameter Q_{sig} for each frequency in the frequency range used. Usually Q_{sig} is constant and does not vary with frequency. Table 2.1 represents the values for Q_{sig} with several different arrays and different frequencies. (All figures and tables appear at the end of the chapter.)

The values of the bandwidth Δf can be found theoretically by plotting the steering angle θ versus frequency. In Figure 2.4 the error bars indicate the -3 dB bandwidth α computed with Equation (2.31) for a 200-element array. At a particular steering direction θ_f, by observing the range of frequencies that overlap, we can determine the bandwidth Δf at that direction. Thus, we can compute Q_{sig} for each frequency, calculate the average, and then find the axial resolution.

2.4.4. Measurement of the axial and lateral resolutions

Figure 2.10 is the spectrogram of three point targets located at respectively (20 m, 9°), (20.05 m, 14°), and (20.1 m, 20°). The lateral resolution, α, is represented by the vertical dashed lines and the axial resolution, Δr, is represented by the horizontal dashed lines.

The simulated phantom used to measure the spatial resolution with the PSF is a very small reflector. Suppose that a point target is placed in the imaging field-of view. With Field II, the emission and reception of the signal by the array are simulated, in a lossless or an attenuating medium. The received signal is processed and the spectrogram of the signal is formed. As an example, Figure 2.11 represents the spectrogram of a target located at r = 15 m and θ = 10°.

The axial resolution can be measured by plotting the column of the spectrogram corresponding to an angle of 10°, as done in Figure 2.12. We restricted the x-axis of the plot to a range of 14.97 m to 15.03 m, where the peak is located. The axial resolution is represented in the figure by an horizontal double arrow and its value is 9 mm. To measure it, we take the range of the two points closest from the –3 dB line (one on the right of the peak, the other on the left) and we subtract them. Thus, for two different experiments, the variation measured for the experimental axial resolution cannot be smaller than the width of a row. The length of the FFT window determines the number of lines in the image and thus the row width. A short window yields narrow rows and a large window yields broad rows. The width of a row can be called row-space resolution. For a window of 50 μs, the row-space resolution is 3.6 mm, whereas for a window of 10 μs, it is only 0.7 mm.

In Figure 2.13 are represented the values of the spectrogram for the row corresponding to a range of 15 m. Only the values between 9° and 11° have been plotted because they correspond to the peak of amplitude. Out of this range, the spectrogram has value below –30 dB and therefore is not relevant for the measurement of the lateral resolution. The –3 dB bandwidth of the peak corresponds to the experimental lateral resolution and can be read directly on the plot. It is represented by an horizontal double arrow and its value is 0.5°. To obtain a numerical value, we take the angle of the two points closest from the –3 dB line (one on the right of the peak, the other on the left) and we subtract them. Therefore, the minimum variation for the beam width we measure is the width of a column. This parameter can be called line-space resolution and it does not depend on the size of the window. It is determined by the processing: a large number of

columns yield very long computations. In the following simulations, the line-space resolution is 0.35°.

2.4.5. Variation of performance with frequency

As we can see in Figure 2.4, the size of the error bars decreases with frequency, so the lateral resolution improves with frequency. Since the lateral resolution is proportional to the wavelength, it is inversely proportional to the frequency and therefore improves with frequency. This is why the spectrogram has a better lateral resolution at the smaller angles, which correspond to higher frequencies. According to Equation (2.38), the axial resolution is inversely proportional to the frequency of the signal, so it too improves at higher frequencies. Figure 2.14 is the spectrogram of two targets located at 7° and 22°, respectively, and we can see that both lateral and axial resolutions are much better for the smaller angle.

2.5. Trade-off Between Axial and Lateral Resolutions

2.5.1. Trade-off due to the processing

From the time-frequency analysis, we can conclude that both the axial and lateral resolutions will depend on the window we use to compute the STFT. The temporal length of the window compared to the duration of the signal is important.

A short window implies a good time localization and therefore good axial resolution. However, since the part of the signal contained in the window is short, we will not get a lot of information about the frequencies contained in it. Thus a short FFT window implies a poor frequency resolution and therefore a poor lateral resolution.

On the other hand, if the temporal window is large, the frequency resolution is good but the time localization is poor; therefore, the image will have a good lateral resolution but a poor axial resolution.

To sum up, the range is determined in the time domain and the angular position in the frequency domain. Since there is a trade-off due to Fourier analysis, there is a trade-off between axial and lateral resolution, depending on the temporal length of the window. This trade-off is due to the processing of the signal and does not depend on the properties of the array. In the following studies, we will choose the size of the window that yields to the best image resolution:

10 μs for a good axial resolution and 100 μs for a good lateral resolution. Primarily, we use a window length of 50 μs, which is a compromise between a large and a short window.

2.5.2. Trade-off between axial and lateral resolution

In addition to the trade-off between axial and lateral resolutions due to the processing of the received signal, there is a trade-off due to the geometry of the beam width. According to Equation (2.37), the axial resolution Δr is inversely proportional to the bandwidth Δf. The bandwidth Δf represents the frequencies contained in the signal coming from an angle θ_f. If the beam width is large, several frequencies are contained in this signal and Δf is large also.

Since the axial resolution depends on Δf, it is related to the beam width also. This explains why the amplitude-steered array can distinguish two points with the same angular position θ but at different ranges. If the beams were infinitely narrow, the signal reflected by a point target would have a single frequency. It implies that two different point targets on the same radial line could not be separated. However, since the beams have a certain width Δf, they overlap and we can determine the distance of the targets. The broader the beams, the better the axial resolution.

In contrast, the lateral resolution is better for narrow beams. We cannot separate two points with the same range and different angular position if their corresponding beams overlap. The thinner the beams, the better the lateral resolution.

Thus, there is a trade-off between lateral and axial resolution depending on the beam width. Importantly, the parameters of the array that change the beam width (e.g., the length of the array) also yield to a trade-off between axial and lateral resolution.

2.5.3. Influence of the length of the array

According to Equation (2.5), the field pattern vanishes for

$$\sin\left[\frac{N}{2}kd(\sin\theta - \sin\theta_0)\right] = 0, \qquad (2.39)$$

and the first values of θ around θ_0 verifying (2.39) are θ^+ and θ^-, such as

$$\theta^{\pm} = \sin^{-1}\left(\sin\theta_0 \pm \frac{\pi}{Nkd}\right). \qquad (2.40)$$

29

The width of the major lobe is defined as the difference between θ^+ and θ^-. Since $\pi/(Nkd)$ decreases when N increases, the width of the major lobe decreases when the number of elements gets larger. Therefore, the length of the array will determine the width of the major lobe, which corresponds to the width of the beam. Figures 2.15 and 2.16 represent plots of the steering angle versus the frequency of the emitted signal for two arrays of different length. We choose an array of 695 elements (15 cm) for Figure 2.15 and an array of $N = 250$ elements (6 cm) for Figure 2.16. The error bars represent the lateral resolution at each frequency, computed according to Equation (2.31), where the number of elements N has to be taken into account. We can see from these plots that the lateral resolution, or beam width, is much better for a large array. In addition, the size of the error bars between the smaller and the larger angles varies only slightly for a large array, but a much more so for a small array. This would yield an important difference in the lateral resolution of the image formed by a small array. The lateral resolution improves when the length of the array is increased. But in the meantime, because the beam width decreases, the range of frequencies that overlap becomes smaller and thus Q_{sig} increases. Therefore, the axial resolution is worsened. With the error bars of Figure 2.15 or 2.16, we can read the bandwidth Δf of the received signal, as we did for Figure 2.4, and compute Q_{sig} and thus the theoretical axial resolution for the different arrays. The values of Q_{sig} for different arrays are reported in Table 2.1. Figure 2.17 is the plot of the theoretical lateral resolution versus the steering angle for three different arrays. Figure 2.18 is the plot of the theoretical axial resolution for the same three arrays. We can see how better the axial resolution is for the smaller array. In contrast, the smaller array has worse lateral resolution.

2.5.4. Broadening of the angular sector

- Single array:

In the previous analysis, the amplitude-steered array insonifies a sector of only 20°. In medical imaging, the field of view may need to be broadened. An image of the entire organ, such as the heart, is more useful for diagnostic applications. The sector insonified in the previous simulations goes from 5° to 25°. The array was steered at a design angle of 5° for a design frequency of 5.6 MHz. The frequencies of the signal range between $f_{start} = 1.2$ MHz and $f_{stop} = 5.6$ MHz. To broaden the field of view up to an angle of 50°, for example, we can choose a smaller frequency f_{start} and keep the same frequency f_{stop}. However, the axial and lateral

resolutions get worse when the frequency decreases, as shown by Equations (2.38) and (2.31). Using low frequencies degrades the quality of the image. Since axial and lateral resolutions have the same variation with the frequency, the following study will focus on the lateral resolution only. The variations of the lateral resolution for an array designed to steer the beam at 5° for a frequency of 5.6 MHz are reported in Table 2.2. They have been computed with Equation (2.31) for an array of 347 elements, a spacing between the elements of 0.126 mm, and a speed of sound of 1500 m/s. The frequency of the chirp goes from 0.64 MHz to 5.6 MHz. For the angles greater than 25°, we obtain a lateral resolution greater than 1°, which is five times greater than the resolution at 5°. Therefore, the image has a quality much worse for the angles greater than 25° than for the smaller angles.

Using higher frequencies for the chirp signal yields a better resolution, as computed in Table 2.3 for an array designed to steer the beam at 5° for a frequency of 11.6 MHz. However, the resolution for the large angles remains poor. For the angles greater than 45°, it is greater than 1°. In addition, there is a big difference in the quality of the image between the smaller and the greater angles. We can conclude that a single array cannot give images of good quality for an angular sector broader than 20°.

- <u>Multiple arrays:</u>

In using several arrays successively, the angular sector swept by the beam can be broadened. The insonified sector depends on the design angle θ_0, the design frequency f_0, and the frequencies f of the chirp signal. Let us suppose that an array is designed to steer the beam to 20° (instead of 5°) for a maximum frequency of 5.6 MHz. When the signal frequency goes from 3.34 MHz to 5.6 MHz, the angular sector swept by the beam goes from 20° to 50°. Since the maximum frequency corresponds to an angle of 20°, the lateral resolution will be optimum for this array at 20°. Suppose now that the array is designed to steer the beam at 35° for the same maximum frequency of 5.6 MHz. When the frequency of the chirp goes from 4.19 MHz to 5.6 MHz, the beam sweeps the angular sector between 35° and 50°. Thus if we use three arrays designed to steer respectively to 5°, 20°, and 35° for the same frequency 5.6 MHz, the angular sector imaged goes from 5° to 50°. Tables 2.2, 2.4 and 2.5 report the values of the lateral resolution computed with Equation (2.31) for these three arrays. The values were computed with Equation (2.31), where the number of elements is 347, the spacing between the elements is 0.126 mm, and the speed of sound is 1500 m/s. As we can see in Table 2.3, the lateral resolution for the

angles from 20° to 35° is much better for the array designed to steer at 20° for a frequency of 5.6 MHz than for the array designed to steer the beam at 5° for the same frequency. The lateral resolution remains smaller than 0.8° for the three arrays, which yields an image of good quality in the entire field of view.

As an example, Figures 2.19 and 2.20 represent the spectrograms formed by a single array and a multiple array respectively. The point targets are located at a range of 2 m. The spacing between the targets is constant and equal to 2°.

Table 2.1 Values of the factor of quality Q_{sig} for different frequencies and for arrays of different lengths. N is the number of elements of the arrays.

Frequency [MHz]	Qsig (N = 200)	Qsig (N = 250)	Qsig (N = 350)
1.2	12.20	20.02	29.92
1.6	12.31	19.88	27.00
2.0	11.77	19.80	28.57
2.4	11.43	19.75	29.75
2.8	11.20	19.71	27.60
3.2	11.43	19.69	26.17
3.6	11.25	19.67	27.08
4.0	11.43	19.65	27.86
4.4	11.28	19.64	26.75
4.8	11.43	19.63	27.41
5.2	11.30	19.62	26.53
5.6	11.22	19.91	27.10

Table 2.2 Theoretical lateral resolution for an array designed to steer at 5° for a maximum frequency of 5.6 MHz.

f (MHz)	5.6	2.8	1.8	1.4	1.15
θ (deg)	5	10	15	20	25
α_{th} (deg)	0.188	0.366	0.558	0.760	0.97
f (MHz)	0.97	0.85	0.75	0.69	0.64
θ (deg)	30	35	40	45	50
α_{th} (deg)	1.20	1.45	1.76	2.07	2.46

Table 2.3 Theoretical lateral resolution for an array designed to steer at 5° for a maximum frequency of 11.6 MHz.

f (MHz)	11.6	5.8	3.9	2.9	2.4
θ (deg)	5	10	15	20	25
α_{th} (deg)	0.087	0.176	0.268	0.365	0.467
f (MHz)	2.4	2.0	1.8	1.4	1.3
θ (deg)	30	35	40	45	50
α_{th} (deg)	0.579	0.702	0.842	1.003	1.19

Table 2.4 Theoretical lateral resolution for an array designed to steer at 20° for a maximum frequency of 5.6 MHz.

f (MHz)	5.6	4.5	3.8	3.3
θ (deg)	20	25	30	35
α_{th} (deg)	0.192	0.247	0.306	0.370

Table 2.5 Theoretical lateral resolution for an array designed to steer at 35° for a maximum frequency of 5.6 MHz.

f (MHz)	5.6	5.0	4.5	4.2
θ (deg)	35	40	45	50
α_{th} (deg)	0.221	0.265	0.316	0.376
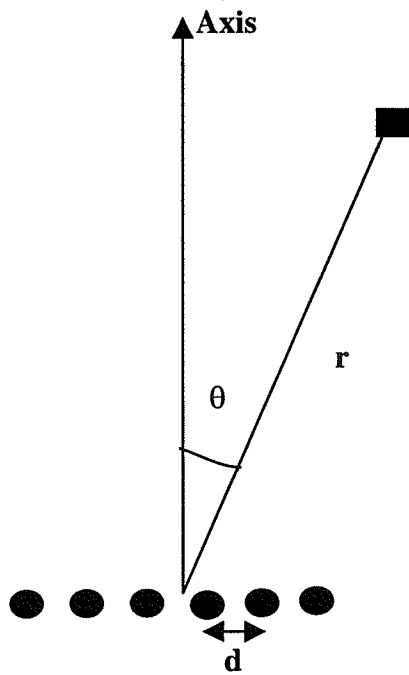
Figure 2.1 Geometry of a linear phased array. The horizontal dots represent the elements of the array and the little square has the polar coordinates (r, θ).
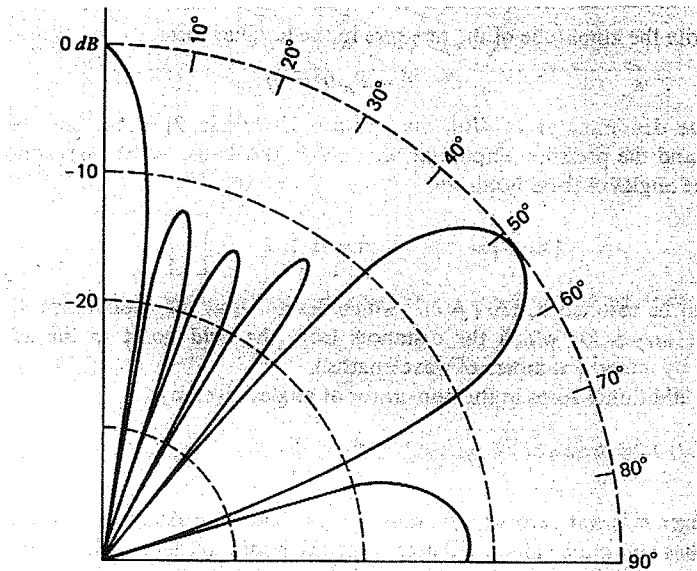
Figure 2.2 Beam pattern for a line array of N in-phase elements radiating sound of wave number k with kd = 8 and N = 5, where d is the spacing between the elements.
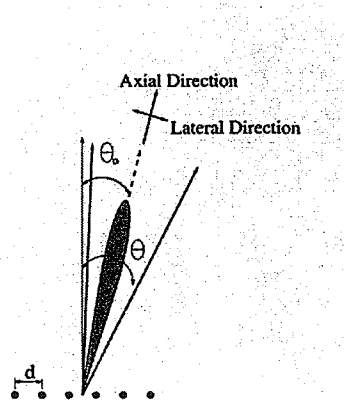
Figure 2.3 Geometry of the amplitude steered array designed to steer at the angle θ_0.
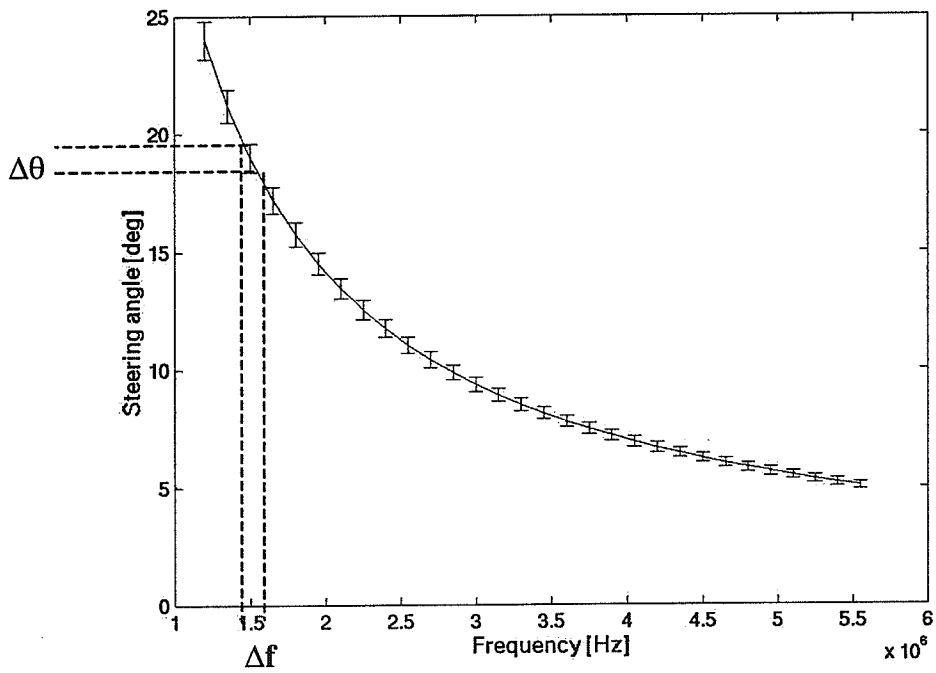
Figure 2.4 Variation of the steering angle with frequency for a 200-element array. The error bars represent the theoretical lateral resolution (beam width) for each frequency. The vertical dashed lines give the corresponding bandwidth Δf.
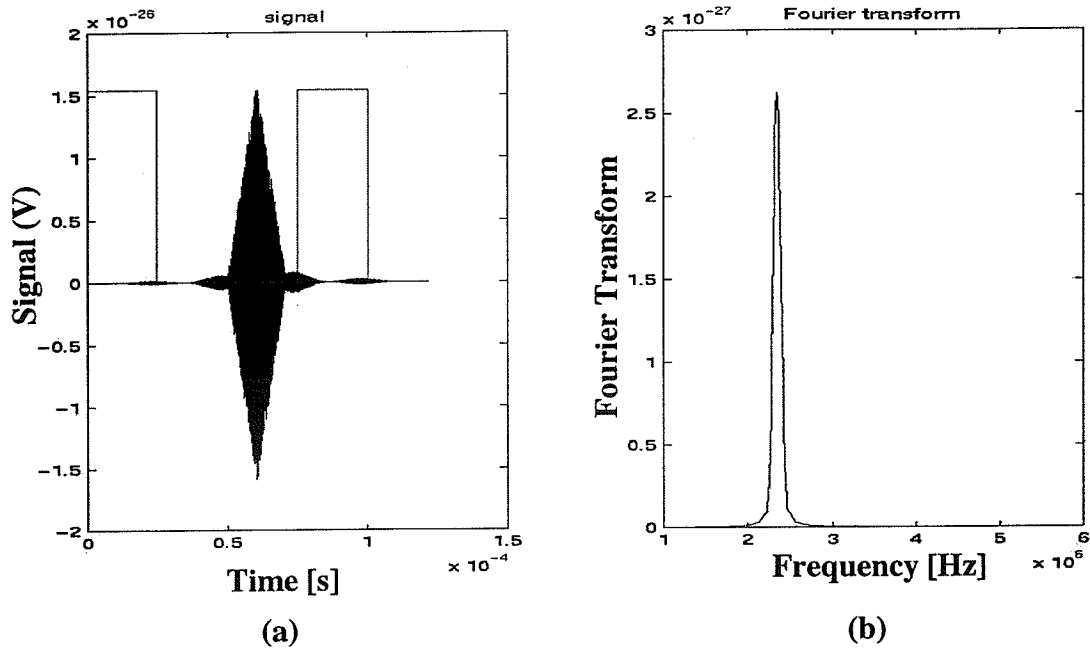
Figure 2.5 (a) Signal reflected by a target with range of 20 cm and an angle of 18°. (b) Fourier transform of the signal. The amplitude array used is designed to steer a beam at 5° for a frequency of 5.6 MHz.
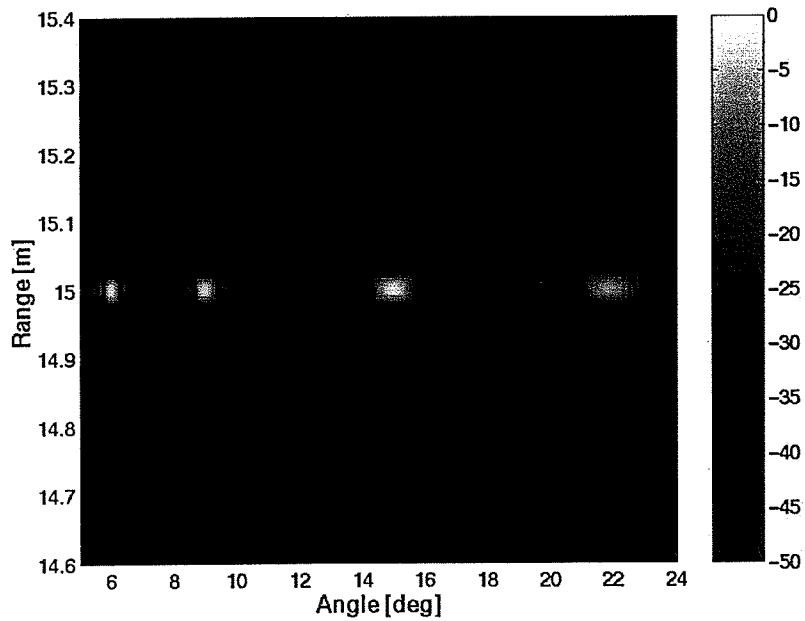
Figure 2.6 Spectrogram of the signal reflected by four targets with the same range of 15 m and with angular frequencies of respectively 6°, 9°, 15°, and 22°.
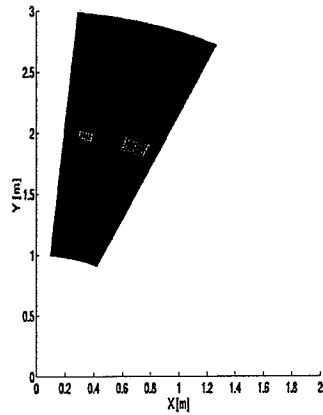
Figure 2.7 Spectrogram of two targets in Cartesian coordinates.
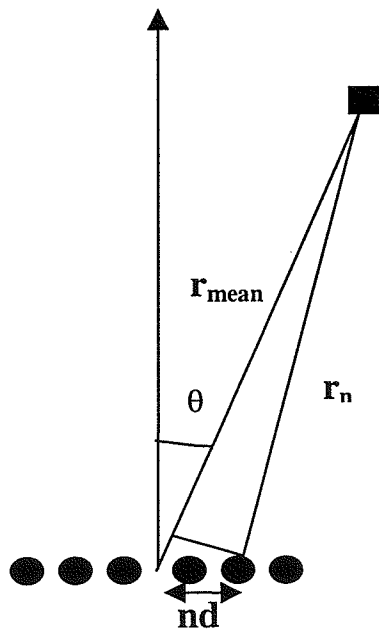
Figure 2.8 Geometry of the array where the target is far from the transducer. d is the spacing between the elements. The approximation $r_n = r_{mean} - nd\sin\theta$ can be used.
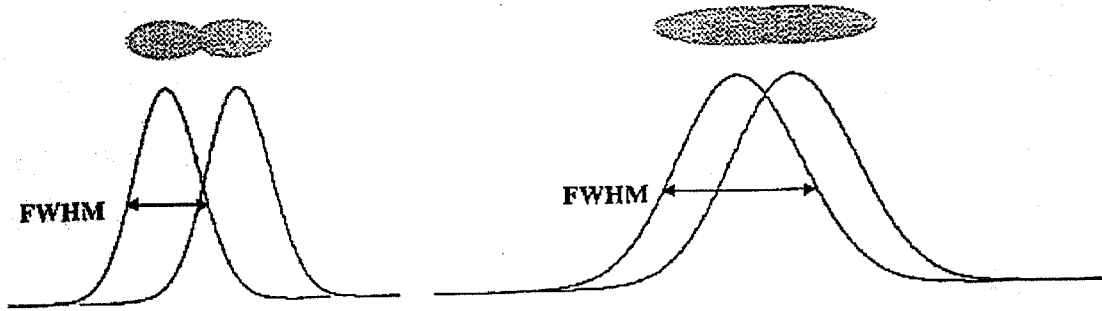
Figure 2.9 Definition of spatial resolution in terms of Rayleigh's criterion. The two point sources on the left are resolvable because their FWHM is smaller than their separation, whereas the point sources on the rigth have a broader PSF and thus cannot be distinguished.
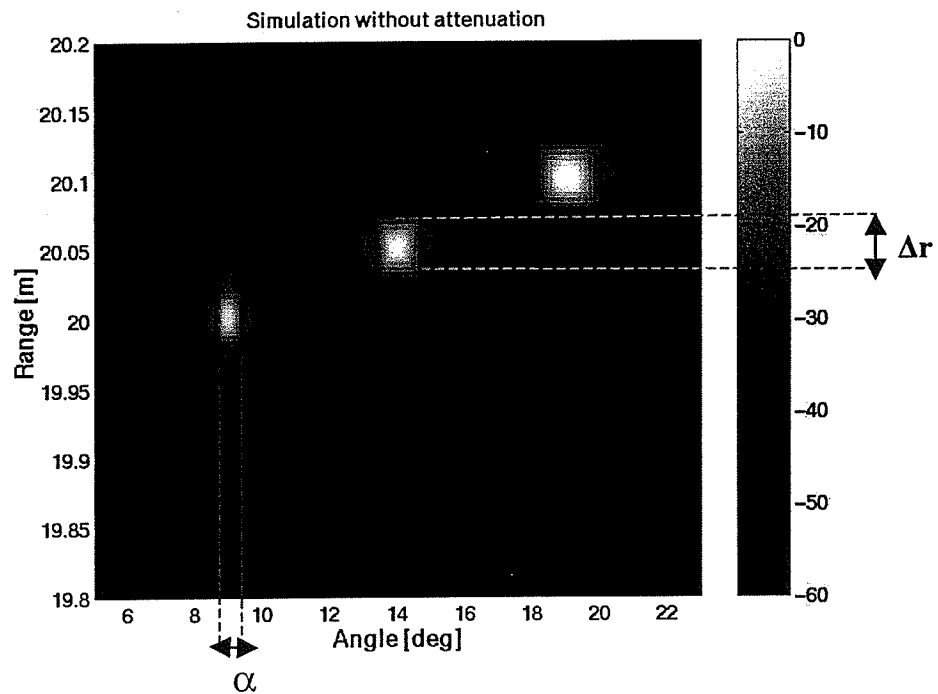
Figure 2.10 Spectrogram of the signal reflected by three targets whose polar coordinates are respectively (20 m, 9°), (20.05 m, 14°), and (20.1 m, 20°). The vertical dashed lines represent the lateral resolution α and the horizontal dashed lines represent the axial resolution.
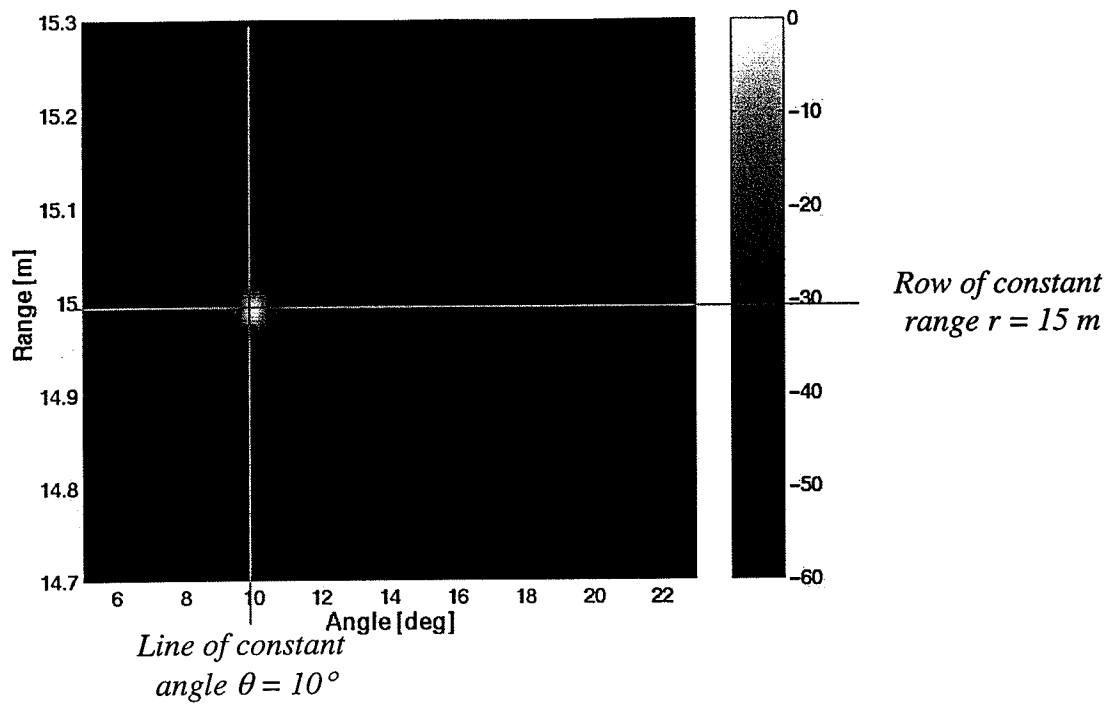
Figure 2.11 Spectrogram of the signal reflected by a target with a range of 15 m and angle 10°.
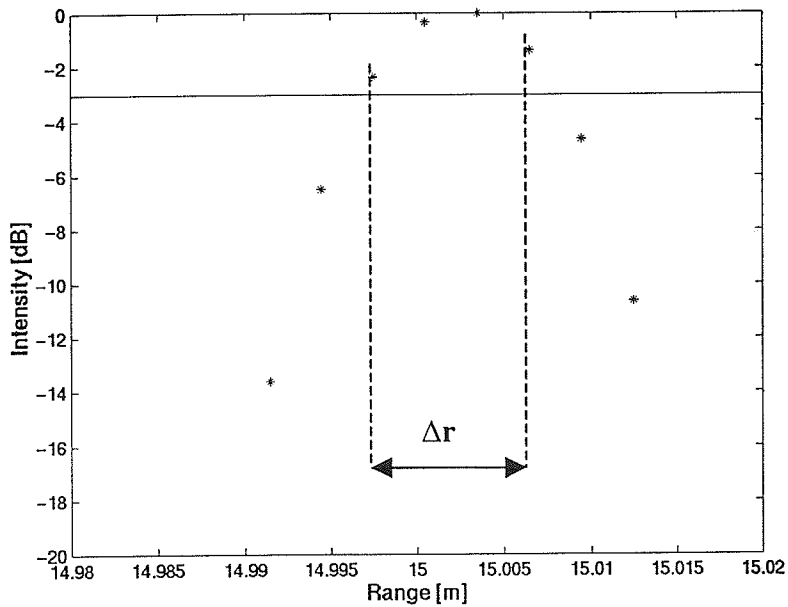
Figure 2.12 Value of the spectrogram of Figure 2.10 for the column corresponding to an angle of 10°. The straight line correspond to the −3 dB bandwidth of the amplitude of the peak. The dashed line represent the experimental axial resolution Δr.
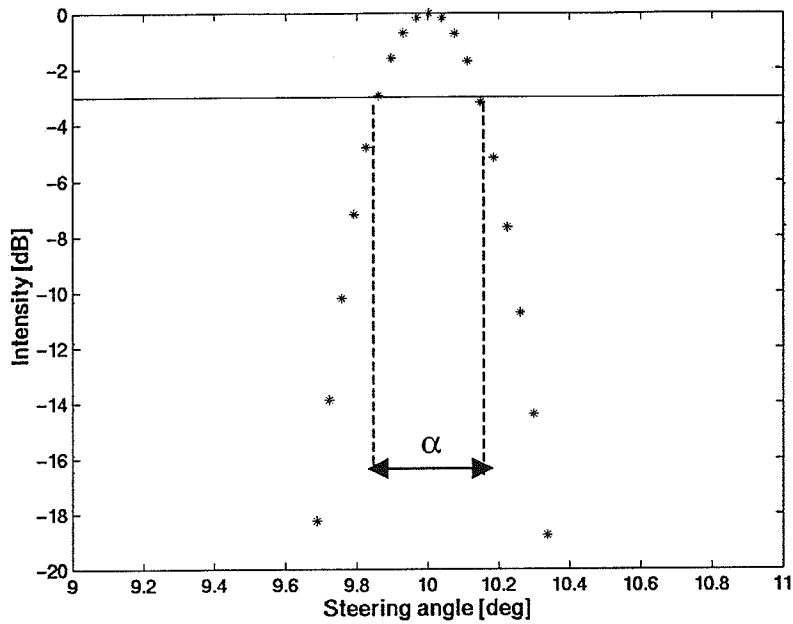
Figure 2.13 Value of the spectrogram on the row of constant range 15 m represented by a horizontal line in Figure 2.10. The straight line corresponds to the –3 dB bandwidth of the amplitude of the peak. The dashed lines represent the experimental lateral resolution α.
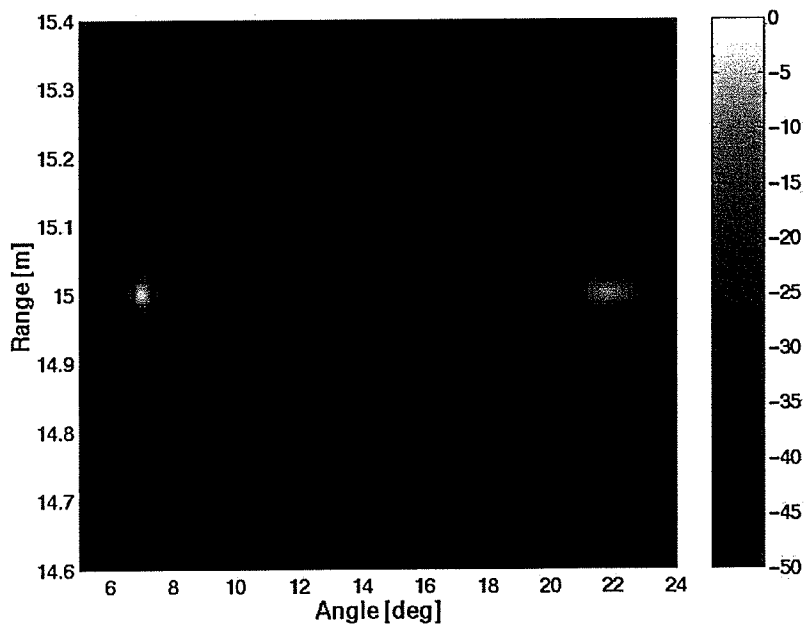
Figure 2.14 Spectrogram of the signal reflected by two point targets with the same range of 15 m and with an angular position of respectively 7° and 22°.
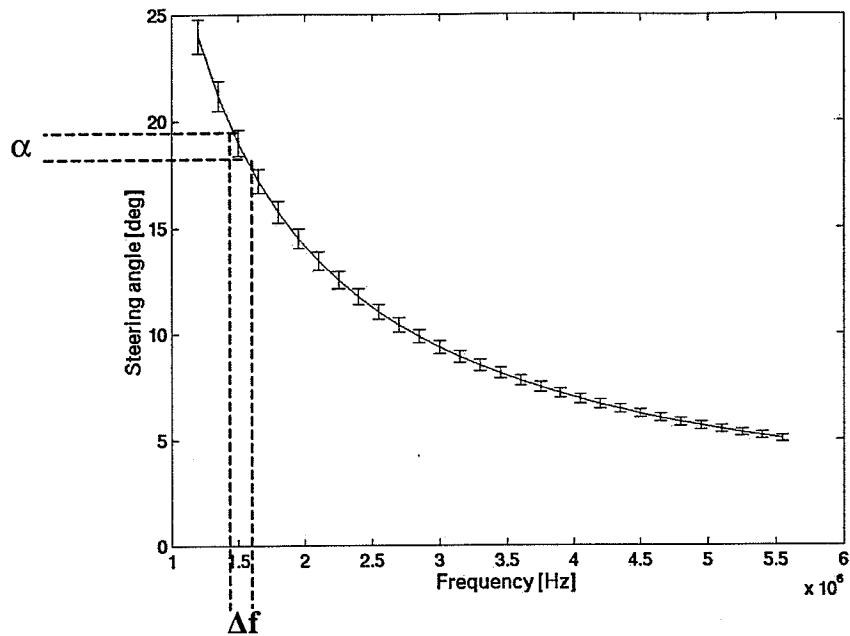
Figure 2.15 Variation of the steering angle versus frequency for an array of 250 elements. The error bars represent the theoretical lateral resolution or beam width α for each frequency. The horizontal dashed lines give α for a frequency of 1.5 MHz. The vertical dashed lines give the corresponding bandwidth Δf.
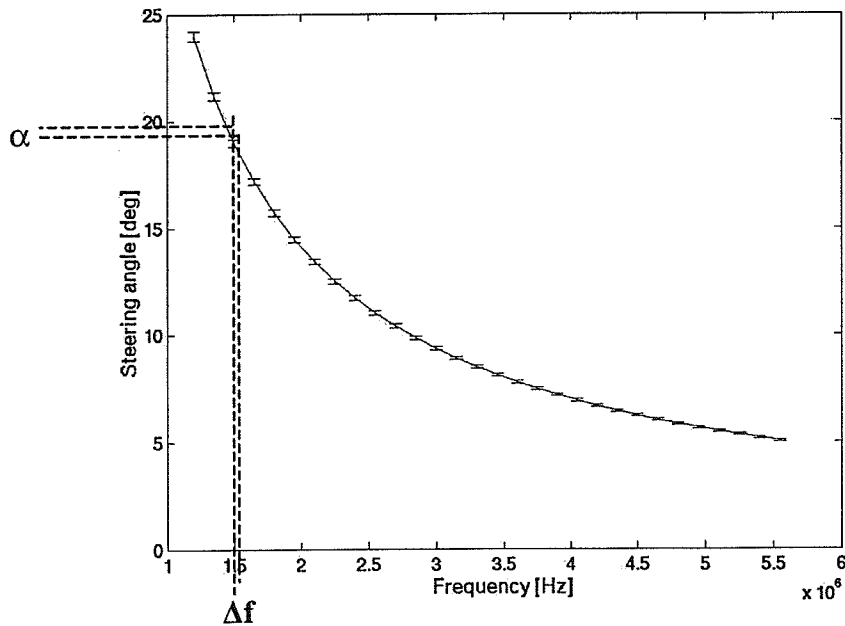
Figure 2.16 Variation of the steering angle versus frequency for an array of 695 elements. The error bars represent the theoretical lateral resolution or beam width α for each frequency. The horizontal dashed lines give α for a frequency of 1.5 MHz. The vertical dashed lines give the corresponding bandwidth Δf.

42
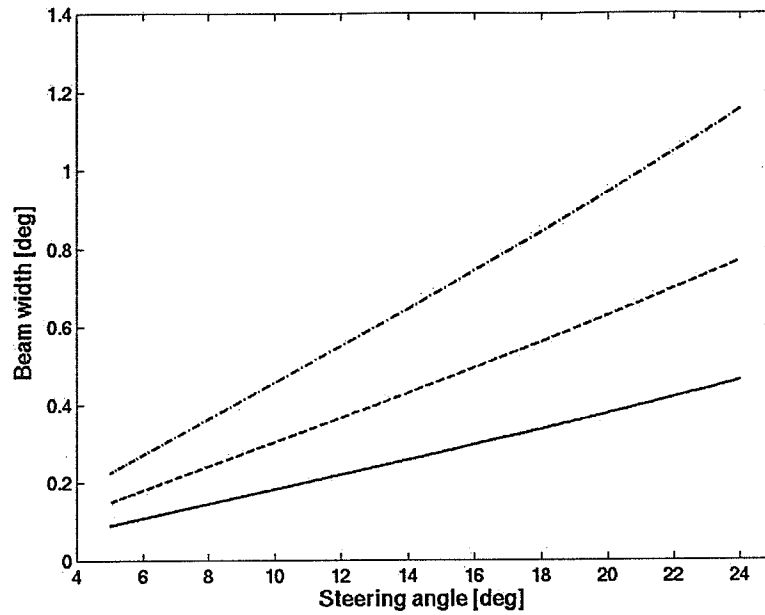
Figure 2.17 Theoretical lateral resolution or beam width for three arrays with lengths of respectively 6 cm (-.-), 9 cm (--), and 12 cm(—).
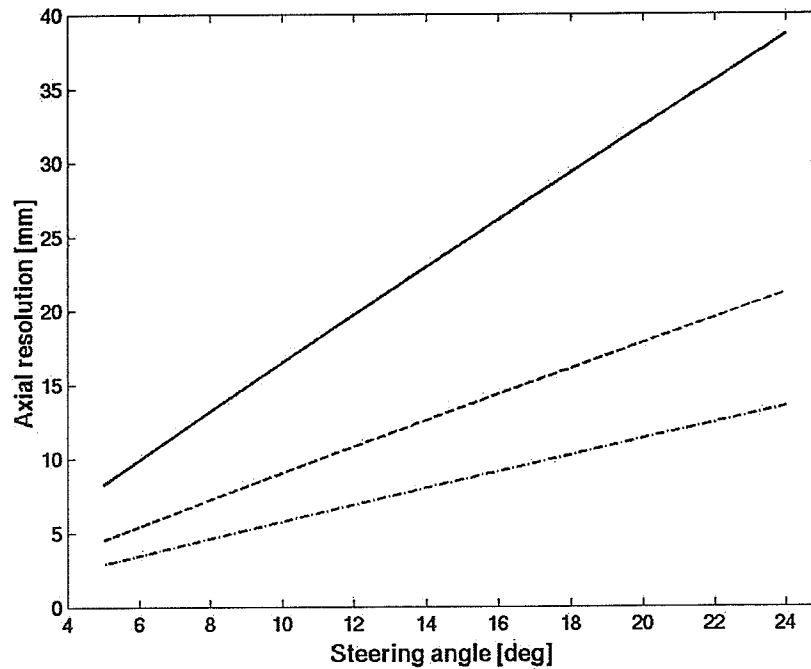
Figure 2.18 Theoretical axial resolution for three arrays with lengths of respectively 6 cm (-.-), 9 cm (--), and 12 cm(—).
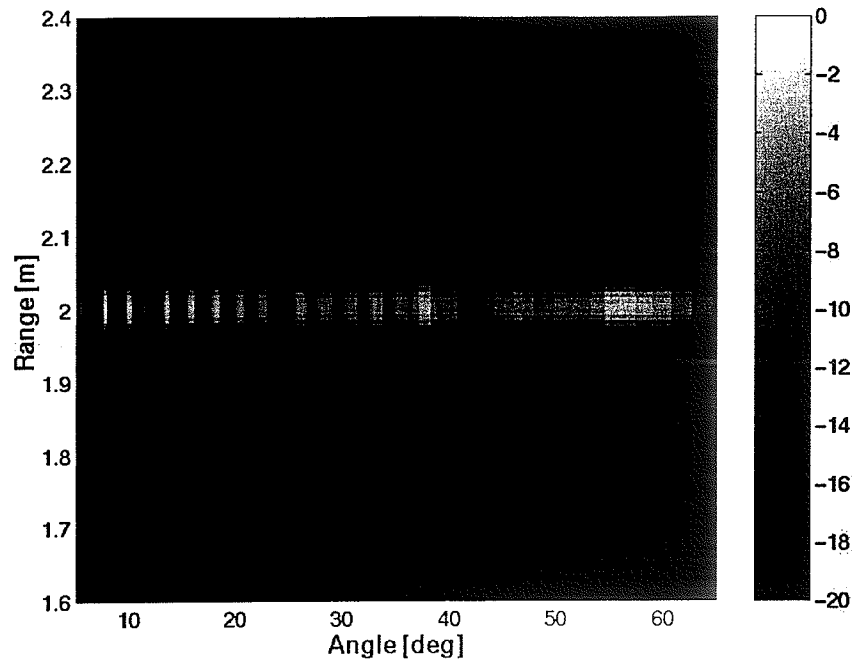
Figure 2.19 Spectrogram of a single array. The point targets are located at a range of 2 m and the spacing between the targets is 2°.
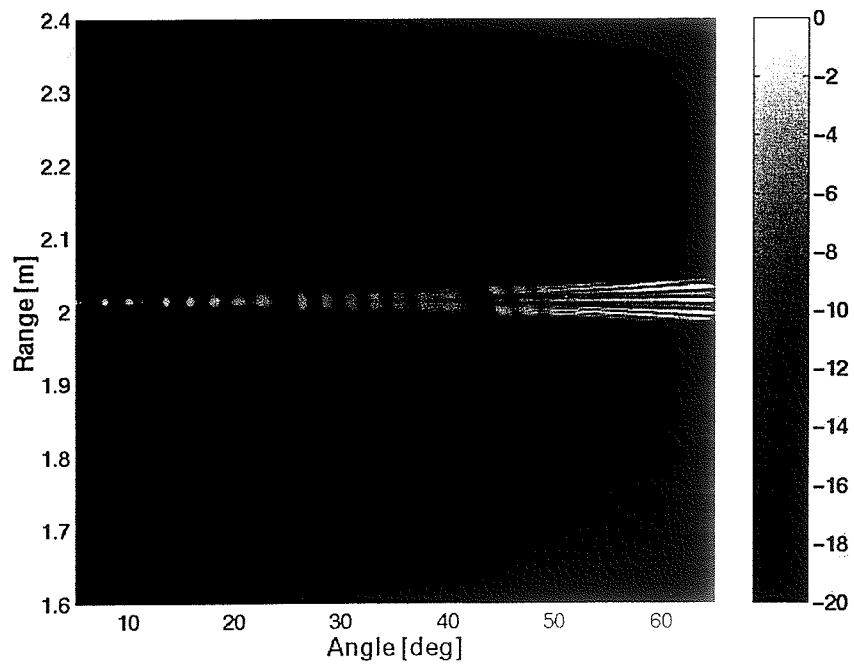
Figure 2.20 Spectrogram of a multiple array. The point targets are located at a range of 2 m and the spacing between the targets is 2°.

CHAPTER 3

RESULTS AND DISCUSSION

This chapter will focus on the performance of the amplitude-steered array when the following parameters are modified: range of the target, length of the array, and attenuation in the medium. First, we will study how the array performs in the near field. Second, the influence of the length on resolution will be examined. Third, the effects of the attenuation in the medium will be studied. And finally, we will see that it is possible to broaden the angular sector swept by the beam by using several arrays successively.

3.1. Performance in the Near Field

In previous studies [*Frazier*, 2000*b*], the amplitude-steered array was used in water and focused to a distance of approximately 20 m. With Equation (2.13), the near field boundary for an array of 7.5 cm and an operating frequency between 1.2 MHz and 5.6 MHz can be evaluated at 4.6 m. The goal of this study is to determine if the array could be used in medical imaging, where the distance of the field of interest is between 5 cm and 30 cm. Indeed, in echocardiography for example, the transducer is on the chest of the patient and the heart is located at a distance of 10 cm to 15 cm [*Hedrick*, 1995] from the transducer. This distance corresponds to the near field for our amplitude-steered array.

Therefore, we will determine how the array performs in the near field by studying the variation of the axial and lateral resolutions. We will then determine up to which distance we can use the array to form images.

3.1.1. Performance for distances between 10 cm and 20 m

To determine up to which range images can be formed with an acceptable resolution, we form the image of a point target located at 20 m, in the far field. The axial and lateral resolution are measured. Then, we redo the experiment for a distance of 10 m and we measure the axial and

lateral resolutions again. We reproduce this experiment for the following distances: 1 m, 50 cm, 30 cm, 25 cm, 20 cm, 15 cm, and 10 cm. Thus, we can study the variation of the performance of the array from the far field to the near field.

A linear amplitude-steered array with the following properties is used:

- Geometry:
    - Number of elements: 347
    - Spacing between the elements: 0.02 mm
    - Width of the elements: 0.106 mm
    - Height of the elements: 0.106 mm
    - Length of the array: 7.5 cm

- Processing:
    - Computation of a $N = 10^{11}$-point FFT.
    - Temporal window of 55 µs (compromise between large and short window)

As an example of these simulations, Figure 2.10 represents the spectrogram of a target located at r = 15 m and θ = 10°. In Figure 2.12 are represented the values of the spectrogram for the row corresponding to a range of 15 m. The lateral resolution is 0.5°. With the same method, the axial resolution can be measured by plotting the column of the spectrogram corresponding to an angle of 10°, as done in Figure 2.11. In Table 3.1 are listed the measurements of the axial and lateral resolution for each simulation. The value of the axial resolution is constant, equal to 9.0087 mm, for the all distances greater than 20 cm. For a distance of 20 cm, the axial resolution is 6.0092. According to Table 3.1, the axial resolution increases as a staircase function and not continuously. This is not due to the transducer but to the processing. The experimental axial resolution cannot be smaller than the width of a row. In the latter experiments, 20 rows represent the sector from 14.906 m to 15.1507 m. Therefore, the width of a row is 2.8 mm. The axial resolution drops from a value of 9.0 mm for a distance of 25 cm to a value of 6.2 mm for a distance of 20 cm. We can check that the difference between 9 mm and 6.2 mm is 2.8 mm, the width of a row.

From these simulations, we can just suppose that the axial resolution improves when the range of the target decreases. Since the axial resolution measured in the far field is only 9.1 mm, a variation of 2.8 mm is not precise enough to determine the performance of the array in the near field.

The lateral resolution is equal to 0.50° for the distances greater than 1 m. It increases to 0.53° for 30 cm and 0.58° for 10 cm. The variation we measure is very limited: 0.58° because the frequency analysis is poor. The window we use is not large enough to describe the variation of the lateral resolution in a field of view below 30 cm.

To sum up, we can conclude from these simulations that the array performs well in the far field (greater than 4 m) and in the near field if the field of view is not too close to the array (greater than 30 cm). To determine the performance of the array in a sector below 30 cm, a further study is necessary.

3.1.2.   Study in the near field with an optimal window

To determine the minimum distance that the amplitude-steered array can image, we study the axial and lateral resolution with an optimal FFT window: a window of 10 μs to measure the axial resolution and a window of 100 μs for the lateral resolution. The measurements are made for ten different distances between 50 cm and 5 cm. The angular position of the target is 10°. The results are reported in Table 3.2.

- Axial resolution:

As explained above, the minimum step size for the variation of the axial resolution is the width of the row in the image. It is determined by the temporal length of the FFT window used to process the signal. With a short window of 10 μs, the width of the row is 0.7 mm. In addition, the time analysis is better than for a window of 50 μs. For a target located at 20 cm, the intensity for the column corresponding to an angle of 10° is plotted in Figure 3.1. The −3 dB line has been plotted also so that the axial resolution can be read. For that range, the axial resolution is 6.15 mm and the height of the side lobes is only −15 dB. Figures 3.2 and 3.3 are similar plots for targets located respectively at 10 cm and 5 cm. The heights of the side lobes do not vary significantly, but the width of the main lobe decreases. For a target located at 5 cm, the axial resolution is 2.4 mm. Thus, the axial resolution improves in the sector close to the array.

- Lateral resolution:

A large window of 100 μs is chosen for the study of the lateral resolution because it gives a better frequency analysis of the received signal. We use the same geometry for the array. The measurements are made for 10 different distances between 50 cm and 5 cm. The angle of the target is 10°. The results are reported in Table 3.2.

Figure 3.4 represents the intensity of the image for the row corresponding to a range of 20 cm. At that range, the lateral resolution can be read on the plot as 0.39°. The height of the side lobes is –8 dB; thus, they are higher than the side lobes in the axial direction. Figure 3.5 is the plot corresponding to a range of 10 cm. The width of the peak is larger, and the –3 dB bandwidth is greater than the one corresponding to a distance of 20 cm. The lateral resolution is 0.52°. The side lobes almost reached a height of –3 dB. Finally, Figure 3.6 represents the intensity of the image versus the steering angle for distance of 7 cm. The shape of the peak is not symmetric anymore, and the intensity of the higher side lobe is above –3 dB. Because of these additional peaks, the dynamic range of the image is reduced. If the height of the side lobes is greater than –3 dB, the image cannot have a good quality. Thus, we can conclude that the amplitude-steered array performs well in the near field as soon as the field of view is located above 10 cm.

3.1.3.   Discussion

From the simulations above, we can conclude that there is a trade-off between lateral and axial resolutions when the study is moved to the near field.

In the far field, the signal emitted by the array can be represented by a single beam steered at a certain angle for a certain frequency. But in the near field, we cannot neglect the influence of the side lobes around the main lobe. We do not apply any apodization to lower the height of the side lobes.

According to the field pattern of the array represented in Equation (2.5), the field vanishes for the angles θ_i such that $\sin[(N/2)kd \ (\sin\theta_i - \sin\theta_0)] = 0$. Therefore, there is a local maximum (side lobe) between each of these nodal planes.

- Axial resolution:

In the near field, the influence of the side lobes cannot be neglected. The signals corresponding to different angular positions, so with different frequencies, overlap. As we have seen previously, the more the beams overlap, the better the axial resolution. If an object is located at an angle θ_0 in the near field, large sidelobes are present and the total reflection also includes contribution the signal corresponding to the angles θ_0^+ and θ_0^- (just after or before the object). They add to the reflected signal corresponding to the beam steered at θ_0, so the signal received will have the shape of a sharp peak and the time resolution will be better.

48

- Lateral resolution:

Because the side lobes at θ_0^+ and θ_0^- contribute to signal corresponding at θ_0^+, the frequency analysis is poor and it will be more difficult to determine the angular position of an object. The peak in amplitude becomes broader and the lateral resolution is worsened.

Figures 3.7-3.9 show the signals received from targets located at 20 cm, 10 cm, and 7 cm, respectively. We can see that the shape of the signal in Figure 3.9 is much sharper than the one in Figure 3.7. Thus, there is a trade-off in the resolutions when the field of view is located below 20 cm.

Actually, the lateral resolution becomes so poor in the region below 20 cm that we have to find some solution to this problem to use the array at these distances.

3.1.4. Solutions

As explained above, the array performs better in the higher frequencies. So, if we keep the same geometry for the array, we can improve the resolution of the images by using higher frequencies. Currently, some linear arrays are used with a frequency of 10 MHz [*Zara et al.,* 2000].

We could also process the image to have good axial and lateral resolutions in the same image. To do that, we could form two images: one with a good lateral resolution, the other with a good axial resolution. Then both images could be processed to obtain one image of good lateral axial quality.

In conclusion, an amplitude-steered array can be used up to a distance of 20 cm if it is operated with a frequency around 5 MHz.

3.2. Variation of the Resolution with the Size of the Array

3.2.1. Experiment with arrays of different length

The length of the array is a parameter that can modify the performance of the array and thus the quality of the spectrogram. To study the resolution of the image with arrays of different lengths, we use a 6 cm array, a 9 cm array, and a 15 cm array. They have the same center to center spacing between the elements, 0.126 mm. Thus the number of elements is respectively

245, 417, and 695. The elements have also the same width and they are rectangle shaped. The steering angle is 5° for 5.6 MHz and there is no attenuation in the medium.

Figures 3.10-3.12 are the spectrograms formed by the 6 cm, 9 cm, and 15 cm arrays, respectively. An FFT window of 50 μs has been used to plot them. They represent three point targets with a range of 50 cm and with angular positions of respectively 8°, 15°, and 22°. By looking at the spectrograms, we can conclude that the length of the array has an influence on the resolution of the image. The axial resolution is better for the 6 cm and 9 cm array than for the 15 cm array. Thus, the smaller arrays yield a better axial resolution. In contrast, the lateral resolution is better for the 15 cm array than for 6 cm or 9 cm array. Thus, the lateral resolution is better for the larger array.

To quantify these observations, the resolutions have been measured for 12 arrays whose lengths range from 3 cm to 15 cm. The size of the elements and their spacing is always the same, along with the frequencies of the excitation signal. However, we use an optimal window to measure the axial and the lateral resolution. For the axial resolution, a window of 10 μs has been chosen. It corresponds to a small window. For the lateral resolution, we chose a large window of 110 μs. The simulations were made with a point target located at a range of 15 m and an angular position of 10°.

The results are reported in Tables 3.3 and 3.4. Figure 3.13 represents the values of the axial resolution at the point (15 m, 10°) versus the length of the arrays used. We can see that the axial resolution is much better for arrays of small length. Figure 3.14 represents the values of the beam width at the point (15 m, 10°) versus the length of the arrays used. As opposed to the axial resolution, the lateral resolution improves when the length of the array is increased.

3.2.2. Discussion

The beam width increases quickly when the length of the array becomes smaller than 7 cm. Indeed, the beam width goes from 0.32° for a length of 7 cm to 0.89° for a length of 3 cm. So, for a difference in the length of $\Delta L = 4$ cm, the difference in the beam width is $\Delta \alpha = 0.57°$. In contrast, the beam width for a length of 14 cm is 0.16°. Thus for a difference in the length of $\Delta L = 8$ cm, the difference in the beam width is only $\Delta \alpha = 0.16°$.

So the variation in the beam width is important for the array smaller than 7 cm, whereas it is not very significant for the arrays larger than 7 cm. The axial resolution varies almost linearly

with the length of the array. For example, for a length L = 11 cm, the axial resolution is 18 mm. Depending of the requirement in resolution that we have, we can determine the maximum allowable length L_{max} of the array. If the quality of the image is considered acceptable for an axial resolution below 20 mm, the maximum length of the array previously studied is $L_{max} = 12$ cm. In the same way, if the lateral resolution should be smaller than 0.4°, the minimum allowable length of the array is $L_{min} = 7$ cm.

3.2.3. Variation of the performance for arrays of different lengths

To study further the difference in the performance for arrays of different size, we can measure the variation of resolutions with the steering angle for three arrays whose lengths are respectively 6 cm, 9 cm, and 15 cm. For these experiments, the same arrays and the same parameters for the processing of the received signal are used.

Figure 3.15 shows the variation of the beam width (or lateral resolution) with the steering angle for the three different arrays. The experimental results (represented by the '*', the 'o' and the '+') match the theoretical results. We can see that the lateral resolution is better for the larger array. For the 15 cm array, the beam width is only 0.08° for a steering angle of 5° and 0.25° for an angle of 24°. The variation with the minimum and the maximum steering angle is not very broad: 0.17°. But for the 9 cm array the beam width is 0.23° for 5° and 0.9° for 24°. The difference in the lateral resolution between the maximum and the minimum steering angle is great: 0.67°. Thus, the quality of the images formed by the smaller array changes significantly throughout the angular sector swept by the beam.

Figure 3.16 is a plot of the axial resolution versus the steering angle. As for the lateral resolution, the measured and calculated values agree well. As opposed to the lateral resolution, the axial resolution is better for short arrays. For the 6 cm array, the axial resolution is only 2.5 mm for a steering angle of 5° and 12.5 mm for 24°. The resolution of the 15 cm array are 8 mm for 5° and 39 mm for 24°. The variation of the axial resolution between the minimum and the maximum angle is only 7 mm for the 6 cm array but 31 mm for the 15 cm array.

For the 9 cm array, the variation of the performance between the minimum and the maximum angle is 0.53° for the beam width and 17.5 mm for the axial resolution. The quality of the image throughout the field of view is relatively uniform.

51

Thus, there is a trade-off between axial and lateral resolution. A large array gives a better lateral resolution and a smaller array gives a better axial resolution.

To conclude, the length of the array is one of the parameters that can modify the beam width. It is an example of the trade-off between axial and lateral resolution due to the beam width. The appropriate length has to be chosen according to the image we want to obtain. If the image is supposed to have a good lateral resolution and if the axial resolution is not a major concern, an array of short length is the best choice. If the image should have a lateral resolution as good as the axial resolution, an array of 9 cm has to be chosen, because it is the compromise between a short and a long array.

If we choose a large array, for example, we can compensate for the poor axial resolution by choosing a small window that improves the axial resolution. For a short array, a large FFT window would be better.

3.3. Variation of the Performance with Attenuation

3.3.1. The problem of an attenuating medium

The amplitude-steered array was initially used under water, to image objects located at approximately 20 m from the array (in the far field). In water, the attenuation coefficient is 0.03 dB/cm/MHz. For a distance of propagation of 20 m, the intensity (in decibels) drops from the initial value I_0 to the value $I_0 - 2.8 \ dB$. Therefore, the attenuation is so small that we can neglect it. But if the array has to be used in medical imaging, the sound has to propagate in the tissues, where the attenuation might be more significant.

As expressed in Equation (2.23), β_{att} is proportional to the frequency. Since the amplitude-steered array spatially separates the frequencies by virtue of the amplitude weighting, the reflected signal coming from the smaller angles (higher frequencies) will be more attenuated than the signal coming from the greater angles (smaller frequencies). Thus, because of the attenuation in the tissues, the angular sector of the spectrogram corresponding to the smaller angles will have a smaller amplitude and the objects located in that region become undetectable if the attenuation is high or if they are too far from the array.

52

3.3.2. Experimental results

The program Field II gives the possibility to simulate the field in an attenuating medium. To obtain quantitative results of the effects of the attenuation on the imaging system, we use the 7 cm array used in part 3.1.2.

Figure 3.17 is the spectrogram of two point targets located at a range of 20 cm and at the angles $\theta_{min} = 10°$ and $\theta_{max} = 20°$ in an attenuating medium. The coefficient of attenuation β_{att} is 0.6 dB/cm/MHz. It can be observed that the intensity of the point representing the target located at $\theta_{min} = 10°$ is much smaller. The wave propagating in the direction closest to the axis has a higher frequency, and thus looses more energy. For the angle of 10°, the frequency $f_1 = 2.8$ MHz and the attenuation coefficient is $\beta_{att}f_1 = 1.68$ dB/cm. For the angle $\theta_{max} = 20°$, the frequency is $f_2 = 1.4$ MHz and the attenuation coefficient is $\beta_{att}f_2 = 0.84$ dB/cm. Thus, after a distance of propagation d = 20 cm, the initial intensity is multiplied by a factor of $exp(-\beta_{att}f_1 d)$ at θ_{min} and by a factor of $exp(-\beta_{att}f_2 d)$ at θ_{max}. The difference in the intensity (in dB) between the two peaks is $(\beta_{att}f_1 - \beta_{att}f_2)d = -17$ dB. This value can be read on the spectrogram.

With a traditional phased array, the angular orientation of the beam emitted by the array does not depend on the frequency. Thus, in an attenuating medium, the intensity depends only on the distance from the array. But with the amplitude-steered array, both the distance and the angular position have to be taken into account.

Figure 3.18 illustrates this property. It is a spectrogram of three targets located respectively at (1 m, 10°), (1.5 m, 15°), and (2 m, 20°). The targets have a different range and a different angular position. The coefficient of attenuation for this simulation is $\beta_{att} = 0.05$ dB/cm/MHz. If the attenuation did not depend on the frequency of the signal, the closest target would be represented in the image by the highest intensity of the spectrogram. However, in Figure 3.18, it can be observed that the point representing the further target is actually the brightest.

Figure 3.19 is a plot of the intensity versus the range for the angle 10°. Three peaks can be observed: the peak at r = 1 m represents the target located at (1 m, 10°). The other peaks are from the two other targets and they are located at 1.5 m and 2 m. Even if the peak at r = 1 m has the highest intensity, its value is very low (-50 dB), and the difference between its intensity and the intensity of the second higher peak is only 50 dB.

53

Figure 3.20 is a plot of the intensity versus range at an angle 15°. The intensity of the higher peak is at 1.5 m and it is still only –25 dB. The difference between the intensity of this peak and the intensity of the second highest peak is also 50 dB.

Finally, Figure 3.21 is the intensity versus the range for an angle of 20°. The peak at 2 m has the maximum intensity, even if the target is located farther away from the array than the other targets. The difference between its intensity and that of the second highest peak is greater: 75 dB. Thus, the effect of the attenuation can be really important, especially if the sector we want to image is close to the array.

3.3.3. Variation of the performance with the steering angle

The axial and lateral resolutions improve with frequency, so the array performs better at the higher frequencies and thus at smaller angles. In an attenuating medium, this property still holds; the resolutions are better for the lower angles. However, there is less difference between the smaller and the larger angles. This means that in an attenuating medium, the array's performance is decreased for the smaller angles. In other words, the relative difference between the resolutions with and without attenuation is greater at the smaller angles. For the axial resolution, the relative difference Δ is defined as

$$\Delta = \left| \frac{\mathrm{AR}_{att} - \mathrm{AR}}{\mathrm{AR}} \right|,$$ (3.1)

where AR_{att} and AR are the axial resolution with and without attenuation, respectively. This property is important because if we try to process the signal to correct for the effects of the attenuation, we have to be aware of the values of the resolutions for the small and large angles. We cannot consider them as constant.

In Figure 3.22, the axial resolution is represented for a medium without attenuation (+) and for an attenuating medium (*). The coefficient of attenuation is $\beta_{att} = 0.5$ dB/cm/MHz. It can be seen that the uncertainty increases for the bigger angles in both cases, but the difference is more pronounced for the smaller angles. For the bigger angles, the resolutions are almost the same.

We can quantify this comment in computing the relative variation of the resolutions. Figure 3.23 is a plot of the relative variation of the axial resolution versus the steering angle. For

54

an angle of 6°, Δ is 25%, whereas for the angles above 12°, it is smaller than 5%. Thus, for the lower angles, the value of the relative variation is high and it drops at about 10°.

3.4. Multiple Arrays

3.4.1. Broadening the angular sector with a single array

In the previous simulations, the angular sector swept by the beam goes from 5° to 25°. If we use a single array, we can broaden the field of view in choosing a lower frequency for f_{start} and keeping the same value for f_{stop}. To sweep the sector between 5° and 65° with a single array designed to steer the beam at 5° for a frequency of 5.6 MHz, the frequency of the chirp must range between 0.53 MHz and 5.6 MHz. The simulations are made with a 347-element array, with a center-to-center spacing between the elements of 0.126 mm. Since both axial and lateral resolutions improve with frequency, the measurements are restricted to the lateral resolution. To process the received signal, we used a window of 100 µs because it optimizes the measure of the lateral resolution.

The results are reported in Table 3.5. Figure 3.24 represents the variation of the lateral resolution for this array, for the angles between 5° and 50°. The straight lines represent the values computed with Equation (2.31) and the '*' the measured values. The results of the simulation match the theoretical values. We can notice that the lateral resolution is very close to the theoretical values for the angles between 5° and 25°. For an angle of 25°, the difference between the experimental and the theoretical values is 0.15°. However, for the angle of 50°, this difference is greater: 0.34°. For the angles greater than 25°, the lateral resolution becomes greater than 1°. The values obtained for the sector between 25° and 50° are too high to give an image of good quality. Figure 3.25 is the spectrogram of four targets located at the same range r = 2 m, but with respective angular positions of 10°, 18°, 35°, and 57°. This picture shows how the lateral resolution is degraded for the angles above 25°. The spectrogram was formed with a window of intermediate length 50 µs; thus, the lateral resolution is worse than the values in Table 3.5 measured using a large window.

In increasing the frequency of the chirp—for example, in designing an array that steers the beam to 5° for a frequency of 11.6 MHz—the lateral resolution is improved. Figure 3.26 represents the variations of the experimental and theoretical lateral resolutions corresponding to

an array designed to steer the beam at 5° for a frequency of 11.6 MHz. As we can see in Table 3.6, the values of the resolutions are much lower. However, for the angles above 40°, the lateral resolution becomes greater than 1°. Therefore, increasing the frequency does not allow one to broaden the angular sector above 40° with the array chosen for the simulations.

3.4.2. Multiple arrays

As explained previously, if several arrays are used successively, the angular sector swept by the beam can be broadened and the lateral resolution remains acceptable. Three arrays of 347 elements have been used. They are designed to steer the beam at respectively 5°, 20°, and 35° for the same frequency 5.6 MHz. For these three arrays, the values of the measured lateral resolution α_{exp} are reported in Tables 3.7-3.9, respectively, along with the theoretical values. If the arrays are operated successively, the field of view goes from 5° to 50° and the lateral resolution remains smaller than 0.8°. Figure 3.27 represents the experimental and the theoretical lateral resolutions for the these three arrays. The arrays have been designed to avoid overlapping between the sector swept. However, the field of view can overlap: in the processing, the signal giving the better resolution, i.e., having the higher frequency for the overlapping sector, is chosen to create the image. As computed in the methodology, with a multiple array, the lateral resolution remains lower than 0.8°, even for the larger angles. We can notice, however, that the difference between theoretical and experimental values is larger for the array sweeping the sector from 35° to 50° than for the array whose steering angle is between 5° and 20°.

Figure 3.28 represents the spectrogram of four targets located at 2 m and with angular positions of 10°, 18°, 35°, and 57°, respectively. To form this image, four arrays have been used successively. Thus, the field of view goes from 5° to 65°. The arrays were designed to steer the beam at respectively 5°, 22°, 35° and 50°. The quality in the image is good, even for the greatest angle, as opposed to the images obtained with a single array.

3.4.3. Discussion

To broaden the angular sector, using a multiple array gives better results than just increasing the frequency of the chirp for two reasons. First, the image has a low lateral resolution throughout the entire field of view, and not only for the larger angles. Second, when we increase the frequency, grating lobes can appear. With an amplitude-steered array whose elements have a

center-to-center spacing d of 0.126 mm, the ratio λ/d is 2.1. Therefore, for a frequency greater than 5.8 MHz, grating lobes are present and they can degrade the quality of the image. However, multiple arrays are electronically more complicated, and they would be more expensive. But the possibility to create fast 2D images of high quality and large field of view is an important advantage of the system and it is unique to the amplitude-steered array.

Table 3.1 Axial and lateral resolution measured for point targets whose range goes from 10 cm to 20 m. An FFT window of 50 μs has been used.

Distance from the array (m)	Axial resolution (mm)	Beam width (deg)
0.010	6.2092	0.5841
0.015	6.2092	0.5522
0.20	6.2092	0.5418
0.25	9.0087	0.5378
0.30	9.0087	0.5378
0.50	9.0087	0.5226
1.00	9.0087	0.5037
10.00	9.0087	0.5037
20.00	9.0087	0.5037

Table 3.2 Axial and lateral resolution measured for point targets whose range goes from 5 cm to 50 cm. An FFT window of 10 μs have been chosen for the axial resolution, and a window of 100 μs has been used for the beam width.

Distance from the array (cm)	Axial resolution (mm)	Beam width (deg)
5.0	2.40	0.5254
7.0	3.11	0.5203
10.0	4.63	0.5153
15.0	5.39	0.4195
20.0	6.15	0.3886
25.0	6.92	0.3703
30.0	6.92	0.3571
35.0	6.92	0.3571
40.0	6.92	0.3571
50.0	6.92	0.3571

Table 3.3 Factor of quality and axial resolution measured for 12 arrays whose lengths range between 3 cm and 14 cm.

Length of the array (cm)	Axial resolution (mm)	Qsig
3	6.4917	11.819
4	8.103	15.913
5	9.7144	20.099
6	11.326	24.399
7	13.34	28.922
8	14.951	33.198
9	16.16	38.354
10	17.771	43.61
11	19.785	49.092
12	21.396	54.123
13	23.411	59.385
14	25.022	64.531

Table 3.4 Number of elements and beam width measured for 12 arrays whose lengths range between 3 cm and 14 cm.

Length of the array (cm)	Beam width (deg)	Number of elements
3	0.89711	139
4	0.65576	186
5	0.49172	232
6	0.49172	278
7	0.32776	325
8	0.32776	371
9	0.24446	417
10	0.24446	463
11	0.24446	510
12	0.24446	556
13	0.16387	602
14	0.16387	649

Table 3.5 Lateral resolution computed (α_{th}) and experimental (α_{exp}) for an array designed to steer the beam to 5° for a frequency of 5.6 MHz.

f (MHz)	5.6	2.8	1.8	1.4	1.15
θ (deg)	5	10	15	20	25
α_{th} (deg)	0.188	0.366	0.558	0.760	0.97
α_{exp} (deg)	0.212	0.385	0.580	0.810	1.12
f (MHz)	0.97	0.85	0.75	0.69	0.64
θ (deg)	30	35	40	45	50
α_{th} (deg)	1.20	1.45	1.76	2.07	2.46
α_{exp} (deg)	1.40	1.65	1.90	2.30	2.80

Table 3.6 Lateral resolution computed (α_{th}) and experimental (α_{exp}) for an array designed to steer the beam to 5° for a frequency of 11.6 MHz.

f (MHz)	11.6	5.8	3.9	2.9	2.4
θ (deg)	5	10	15	20	25
α_{th} (deg)	0.087	0.176	0.268	0.365	0.467
α_{exp} (deg)	0.190	0.190	0.291	0.403	0.475
f (MHz)	2.0	1.8	1.6	1.4	1.3
θ (deg)	30	35	40	45	50
α_{th} (deg)	0.579	0.702	0.842	1.003	1.19
α_{exp} (deg)	0.586	0.725	0.940	1.103	1.370

Table 3.7 Lateral resolution computed (α_{th}) and experimental (α_{exp}) for an array designed to steer the beam to 5° for a frequency of 5.6 MHz.

f (MHz)	5.6	2.8	1.8	1.4
θ (deg)	5	10	15	20
α_{th} (deg)	0.188	0.366	0.558	0.760
α_{exp} (deg)	0.212	0.385	0.580	0.795

Table 3.8 Lateral resolution computed (α_{th}) and experimental (α_{exp}) for an array designed to steer the beam to 20° for a frequency of 5.6 MHz.

f (MHz)	5.6	4.5	3.8	3.3
θ (deg)	20	25	30	35
α_{th} (deg)	0.192	0.247	0.306	0.370
α_{exp} (deg)	0.220	0.262	0.351	0.422

Table 3.9 Lateral resolution computed (α_{th}) and experimental (α_{exp}) for an array designed to steer the beam to 35° for a frequency of 5.6 MHz.

f (MHz)	5.6	5.0	4.5	4.2
θ (deg)	35	40	45	50
α_{th} (deg)	0.221	0.265	0.316	0.376
α_{exp} (deg)	0.231	0.292	0.351	0.432
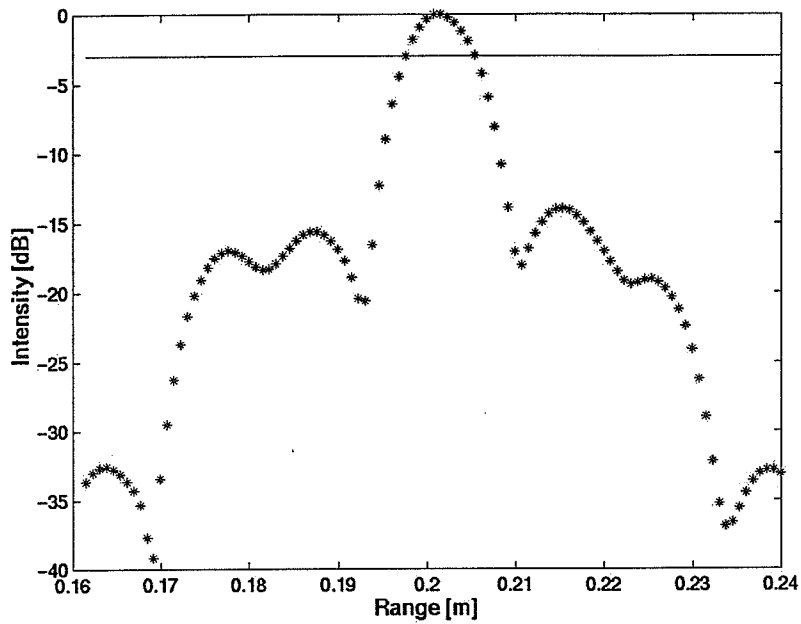
Figure 3.1 Values of the spectrogram for the column corresponding to an angle of 10°. The signal is reflected by a target located at (20 m, 10°).
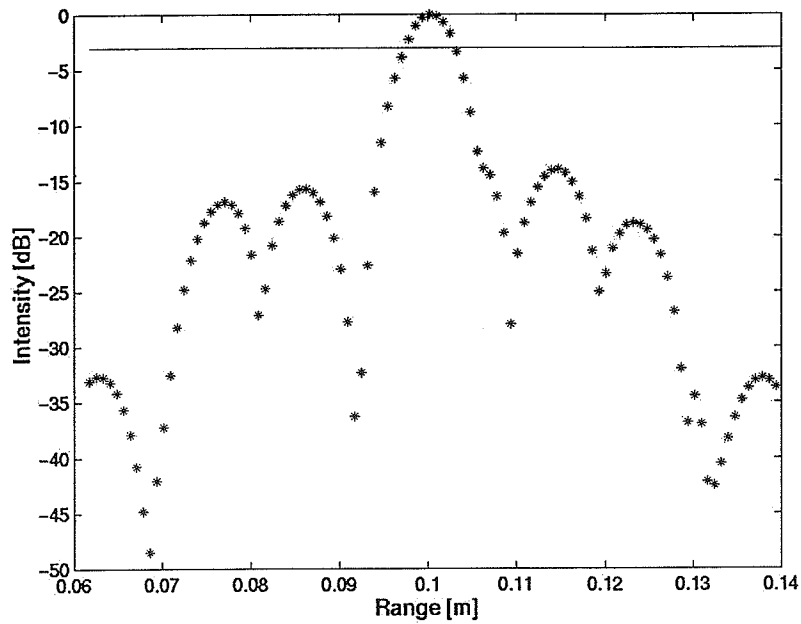
Figure 3.2 Values of the spectrogram for the column corresponding to an angle of 10°. The signal is reflected by a target located at (10 cm, 10°).
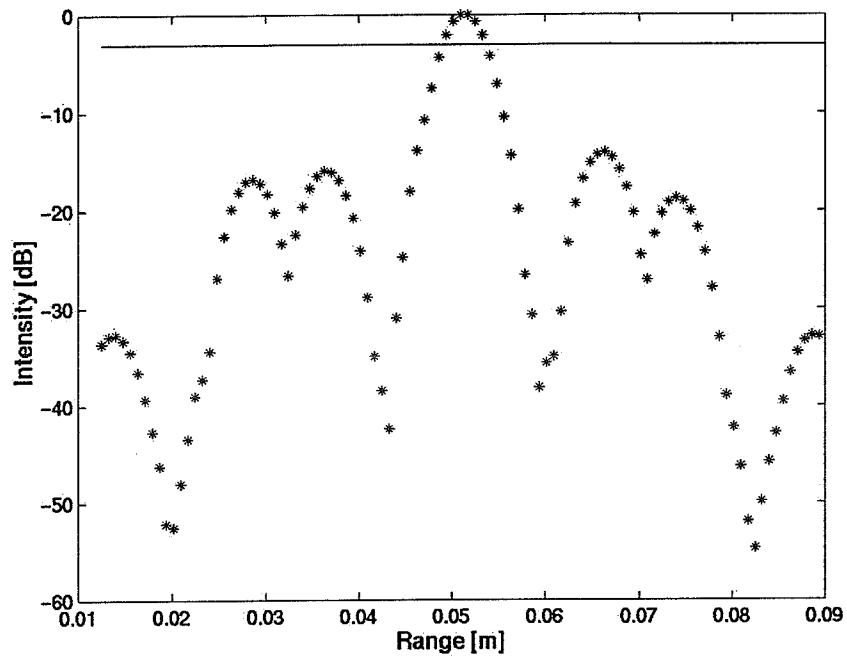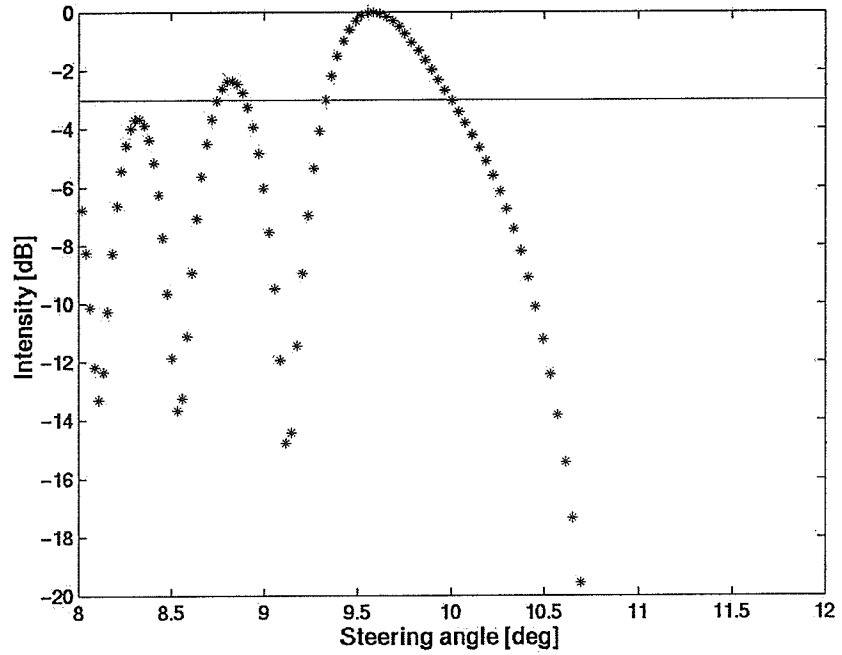
Figure 3.3 Values of the spectrogram for the column corresponding to an angle of 10°. The signal is reflected by a target located at (5 cm, 10°).
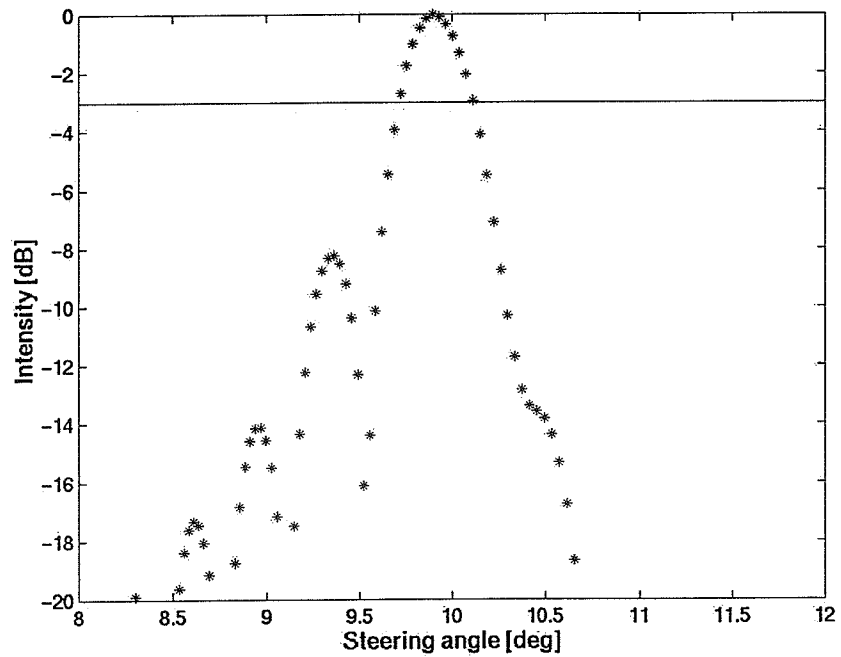
Figure 3.4 Value of the spectrogram for the row corresponding to a range of 20 cm. The signal is reflected by a target located at (20 cm, 10°). The straight line represents the –3 dB bandwidth.
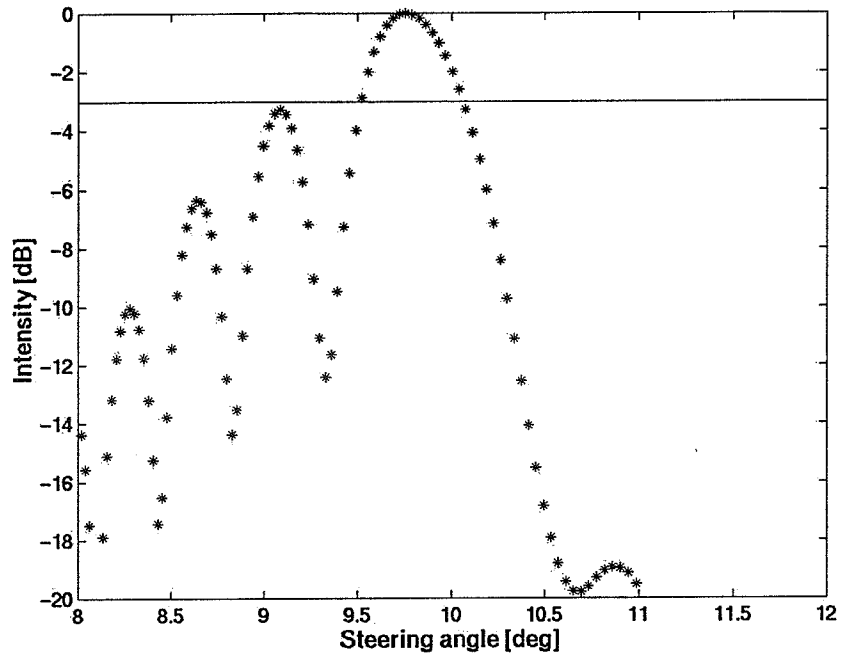
Figure 3.5 Value of the spectrogram for the row corresponding to a range of 10 cm. The signal is reflected by a target located at (10 cm, 10°).

Figure 3.6 Value of the spectrogram for the row corresponding to a range of 7 cm. The signal is reflected by a target located at (7 cm, 10°).
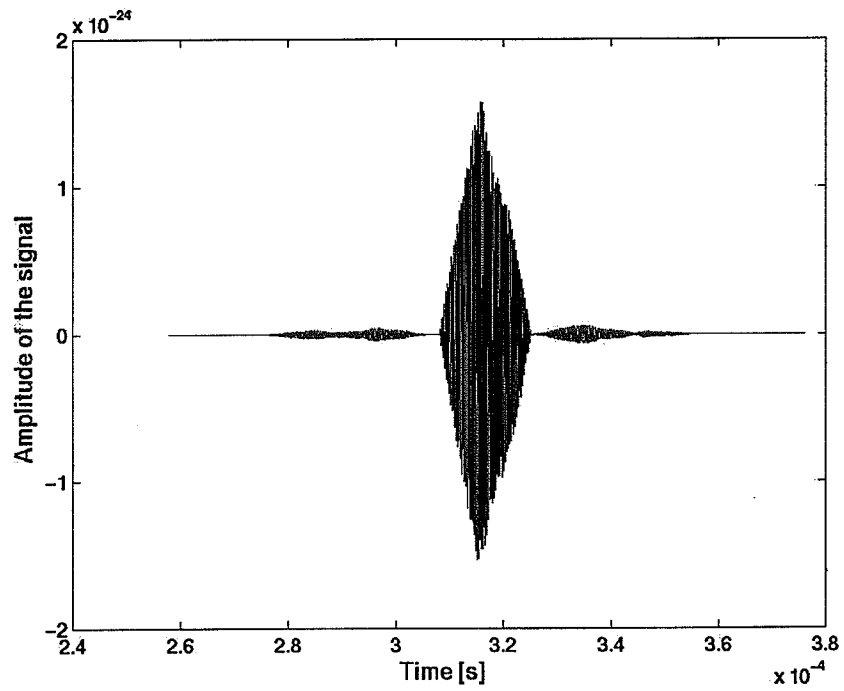
Figure 3.7 Amplitude of the signal reflected by a target located at 20 cm.
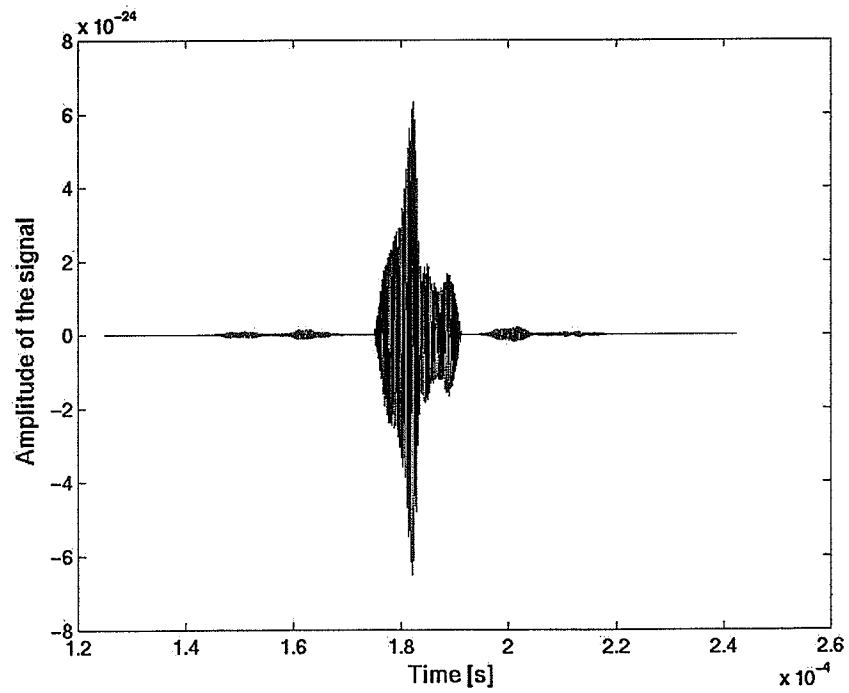
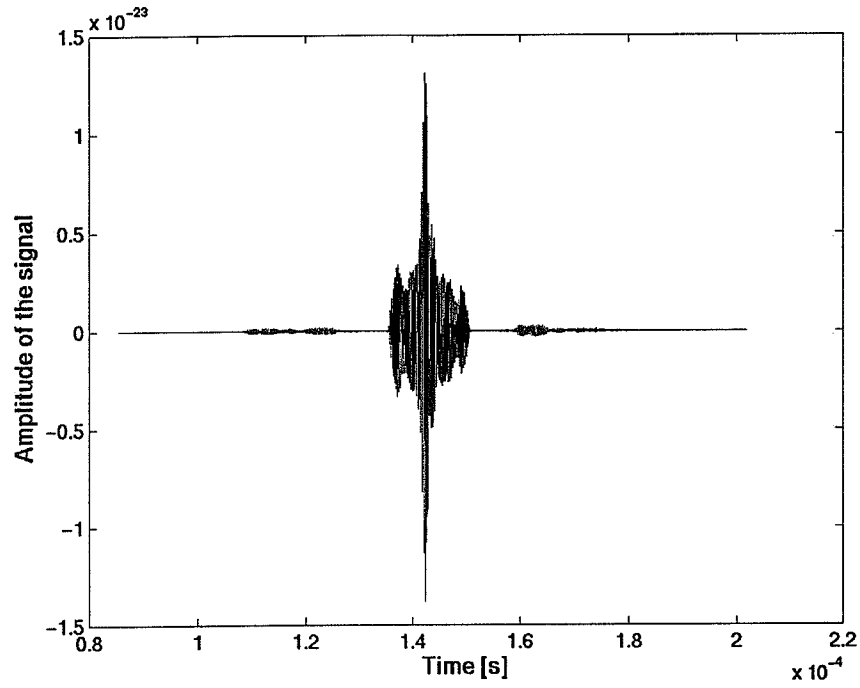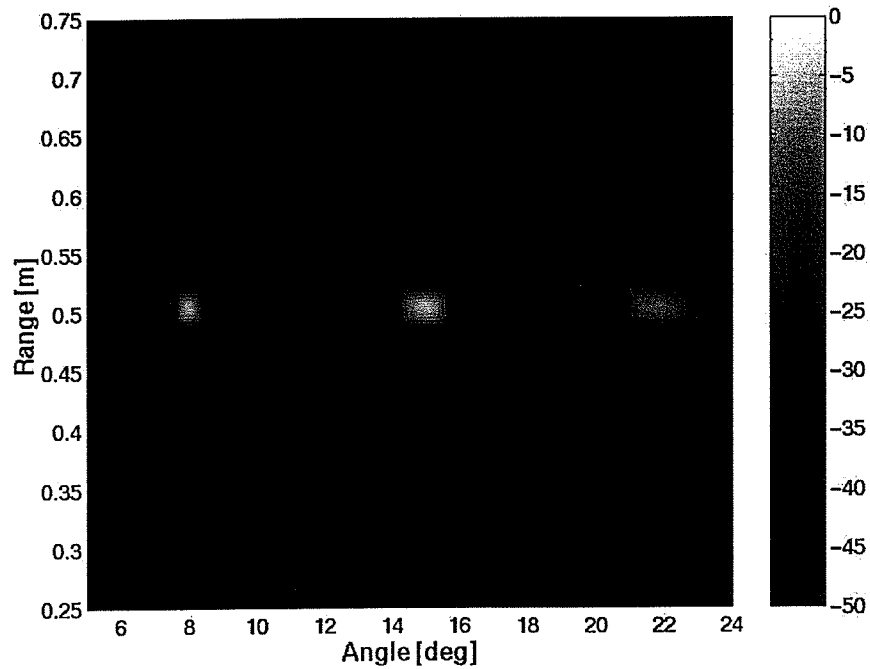Figure 3.8 Amplitude of the signal reflected by a target located at 10 cm.

Figure 3.9 Amplitude of the signal reflected by a target located at 7 cm.

Figure 3.10 Spectrogram of three targets with polar coordinates (50 cm, 8°), (50 cm, 15°), and (50 cm, 22°). The length of the array used is 6 cm.
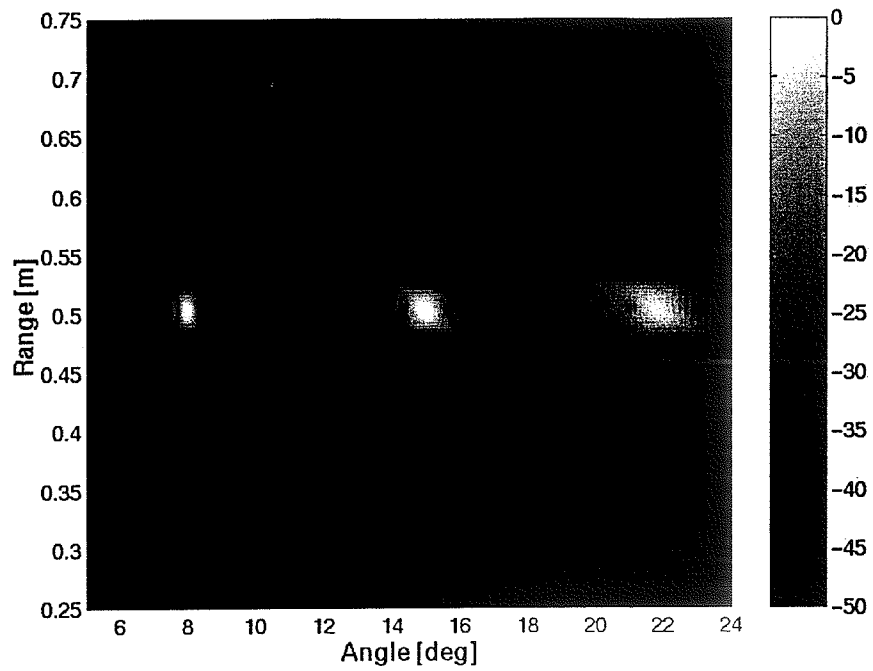
Figure 3.11 Spectrogram of three targets with polar coordinates (50 cm, 8°), (50 cm, 15°), and (50 cm, 22°). The length of the array used is 9 cm.
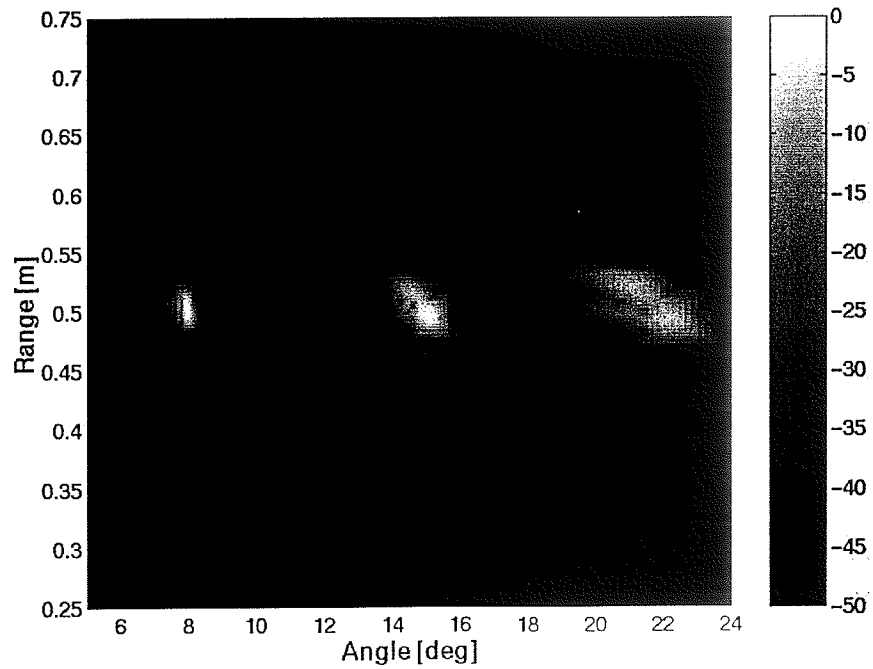

Figure 3.12 Spectrogram of three targets with polar coordinates (50 cm, 8°), (50 cm, 15°), and (50 cm, 22°). The length of the array used is 15 cm.
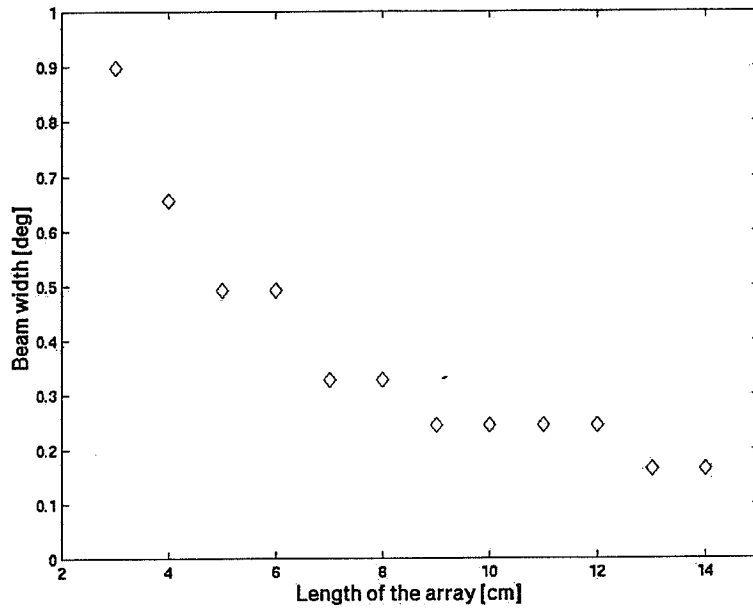
Figure 3.13 Axial resolution measured for 12 arrays whose lengths range between 3 cm and 15 cm. The simulations were realized with a point target located at a range of 15 m and an angular position of 10°.
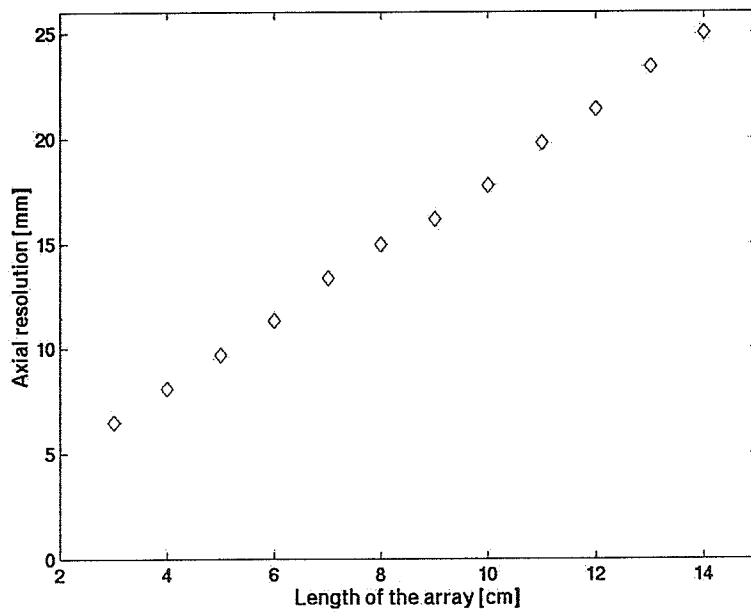

Figure 3.14 Lateral resolution measured for 12 arrays whose lengths range between 3 cm and 15 cm. The simulations were realized with a point target located at a range of 15 m and an angular position of 10°.
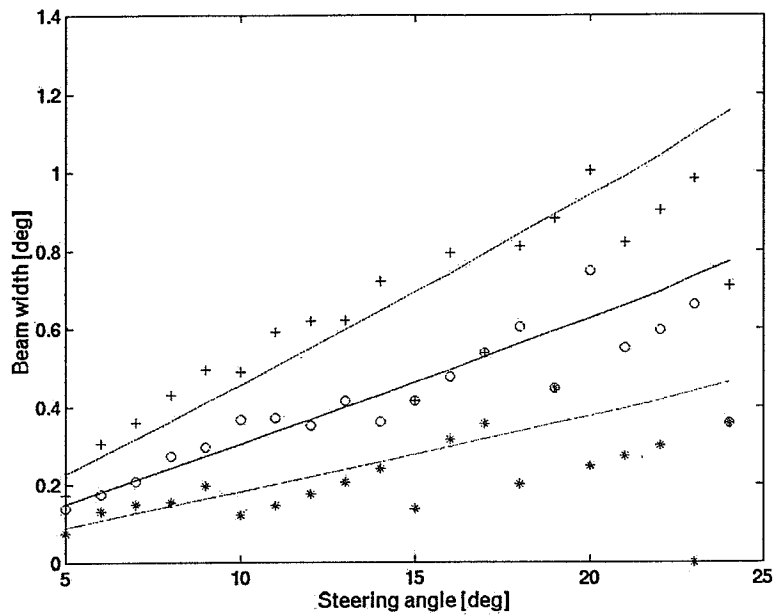
Figure 3.15 Variation of the beam width with the steering angle for three different arrays. '*', 'o', and '+' represent the variation of respectively a 15 cm array, a 9 cm array and a 6 cm array.
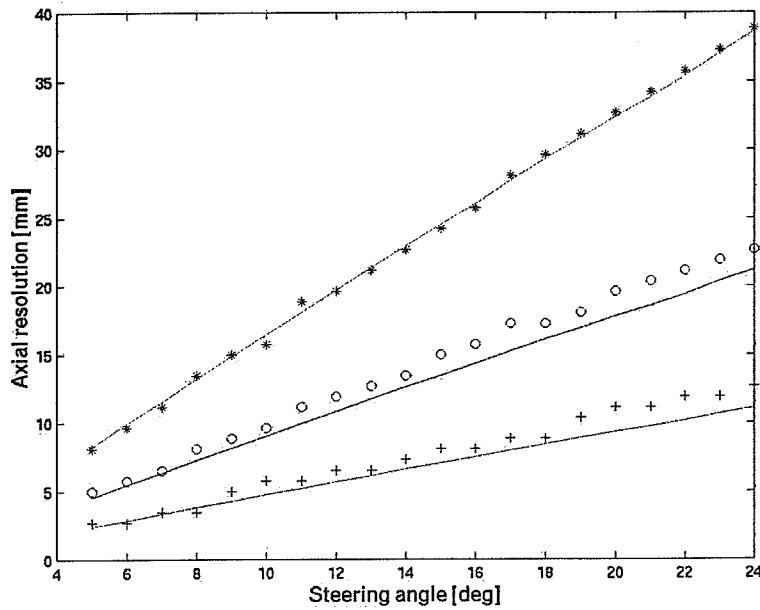

Figure 3.16 Variation of the axial resolution with the steering angle for three different arrays. '*', 'o', and '+' represent the variation of respectively a 15 cm array, a 9 cm array and a 6 cm array.
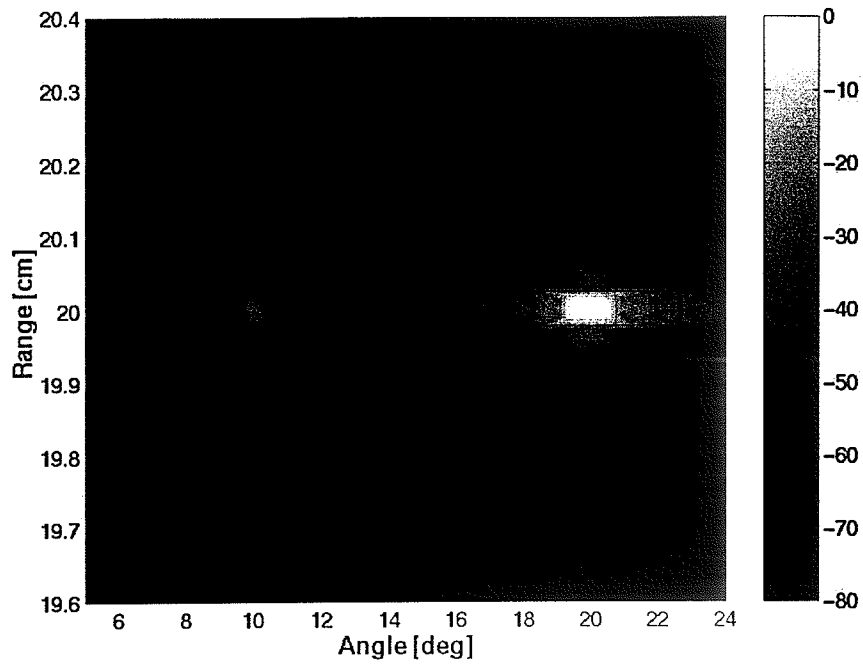
Figure 3.17 Spectrogram of two targets located at a range of 20 cm and with angular position respectively 10° and 20°. The medium is attenuating and the coefficient of attenuation is 0.6 dB/cm/MHz.
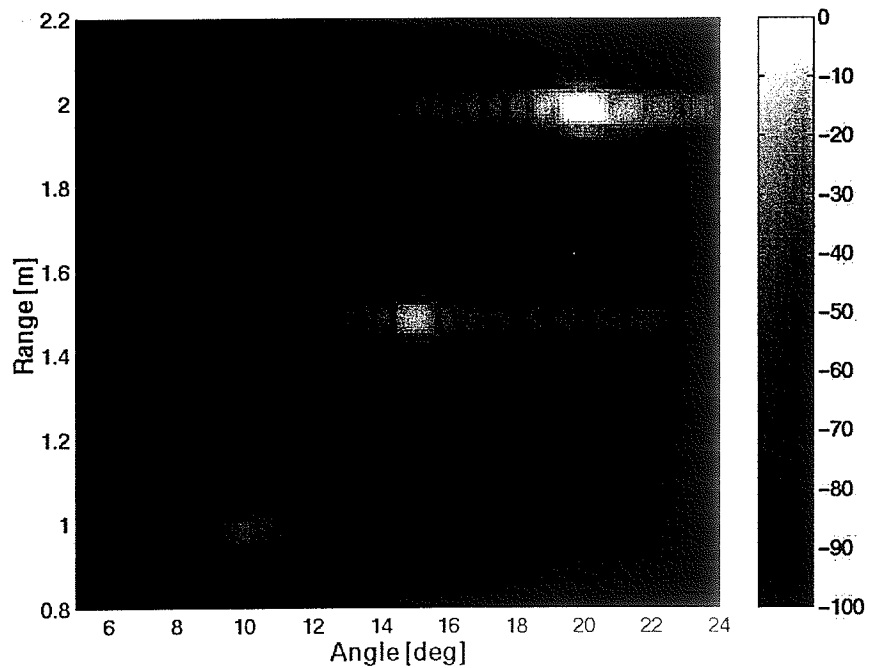

Figure 3.18 Spectrogram of three targets in an attenuating medium (β_{att} = 6 dB/cm/MHz). Their polar coordinates are (1 m, 10°), (1.5 m, 15°), and (2 m, 20°).

Figure 3.19 Intensity of the spectrogram represented in Figure 3.18 versus range for the column corresponding to an angle of 10°.

Figure 3.20 Intensity of the spectrogram represented in Figure 3.18 versus range for the column corresponding to an angle of 15°.
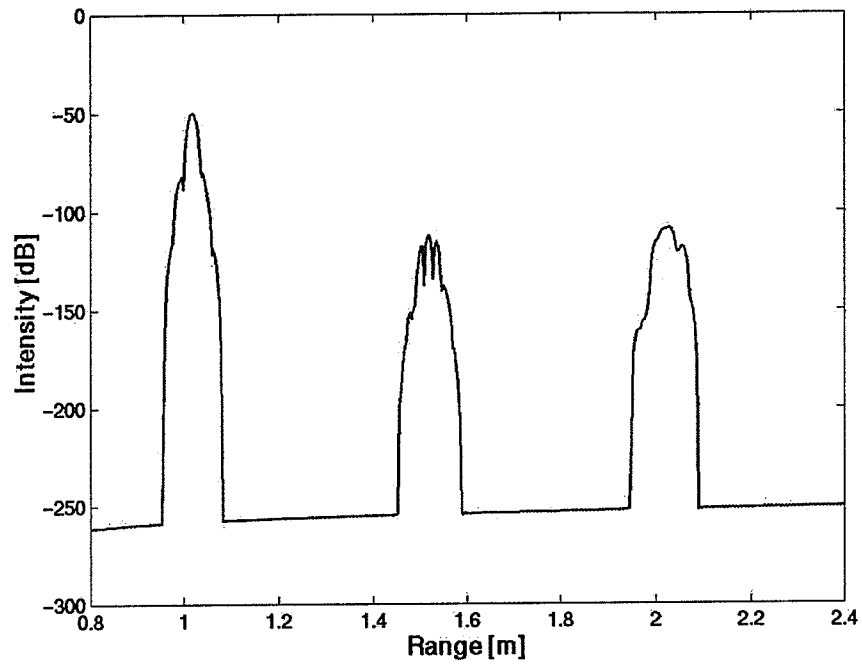
71
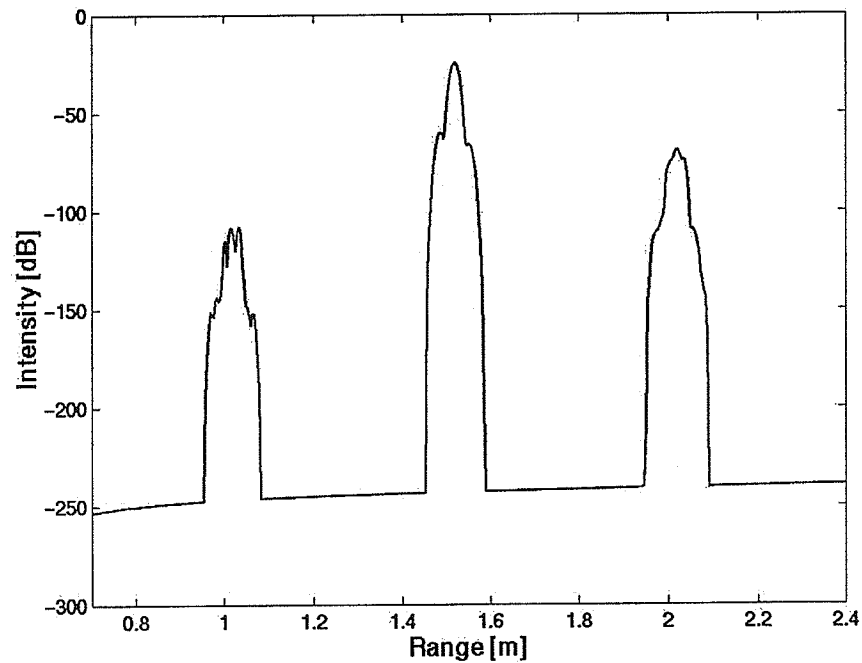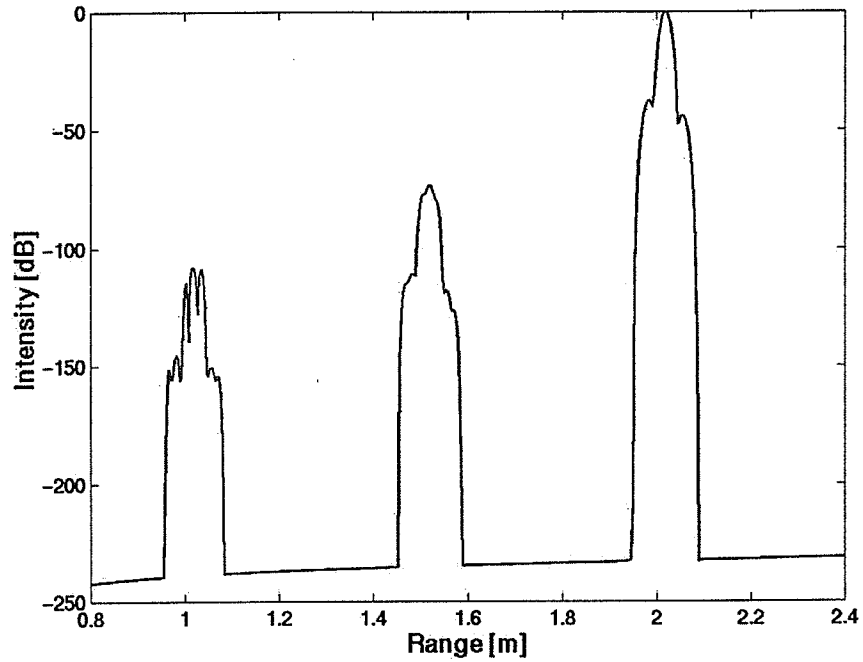
Figure 3.21 Intensity of the spectrogram represented in Figure 3.18 versus range for the column corresponding to an angle of 20°.
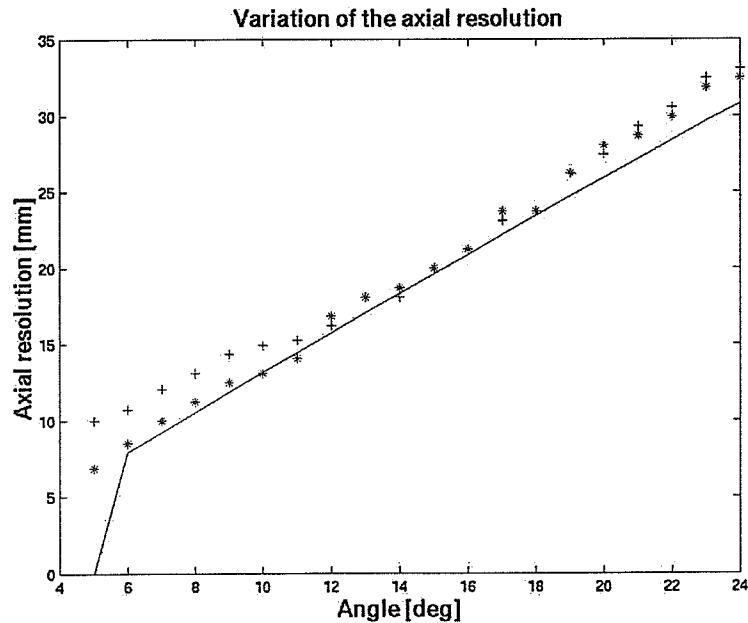
Figure 3.22 Variation of the axial resolution versus the steering angle in an attenuating medium (β_{att} = 6 dB/cm/MHz) ('+') and in a nonattenuating medium ('+'). The straight line represents the theoretical values of the axial resolution.

72

Relative variation of the axial resolution
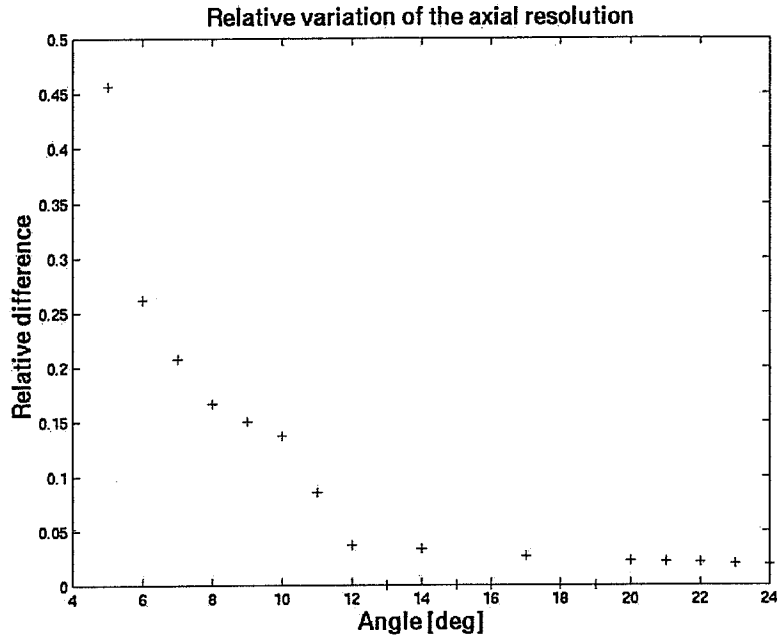
Figure 3.23 Relative variation of the axial resolution. The coefficient of attenuation of the attenuating medium is $\beta_{att} = 6$ dB/cm/MHz.

Figure 3.24 Variation of the lateral resolution with the steering for a single array designed to steer the beam at 5° for a frequency of 5.6 MHz. The theoretical results are represented by the straight line, the experimental results are represented by the '*'.
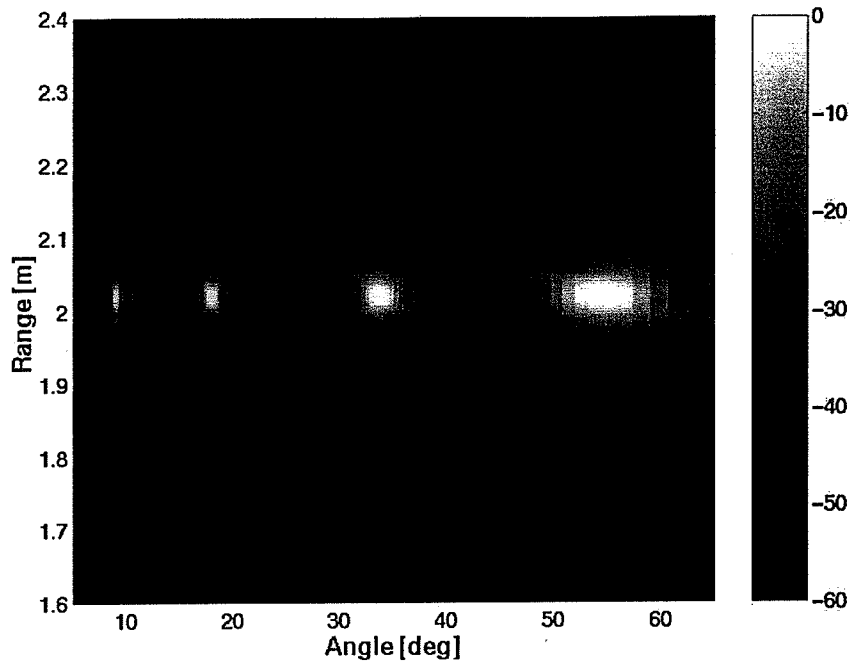
Figure 3.25 Spectrogram of four point targets for a single array designed to steer to 5° for a frequency of 5.6 MHz. The targets have the same range of 2 m and their polar coordinates are respectively 10°, 18°, 35°, and 57°.
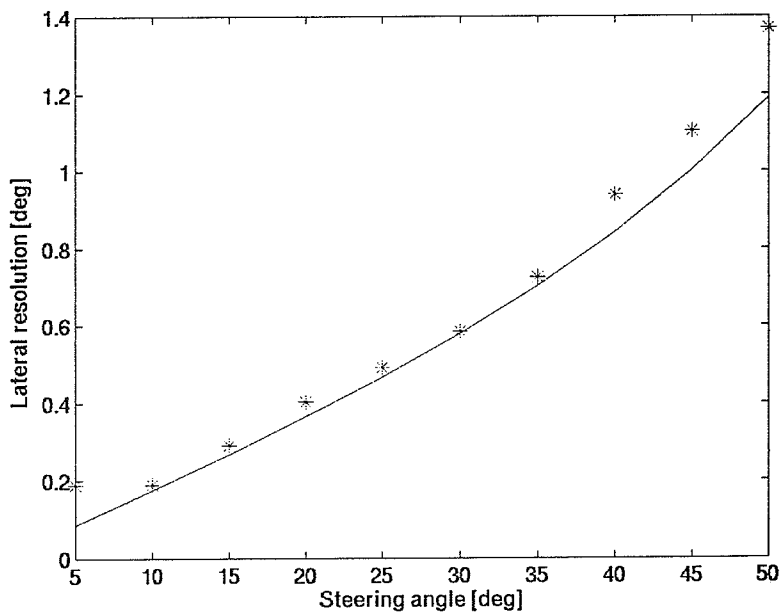
Figure 3.26 Variation of the lateral resolution with the steering for a single array designed to steer the beam at 5° for a frequency of 11.6 MHz. The theoretical results are represented by the straight line, the experimental results are represented by the '*'.

74

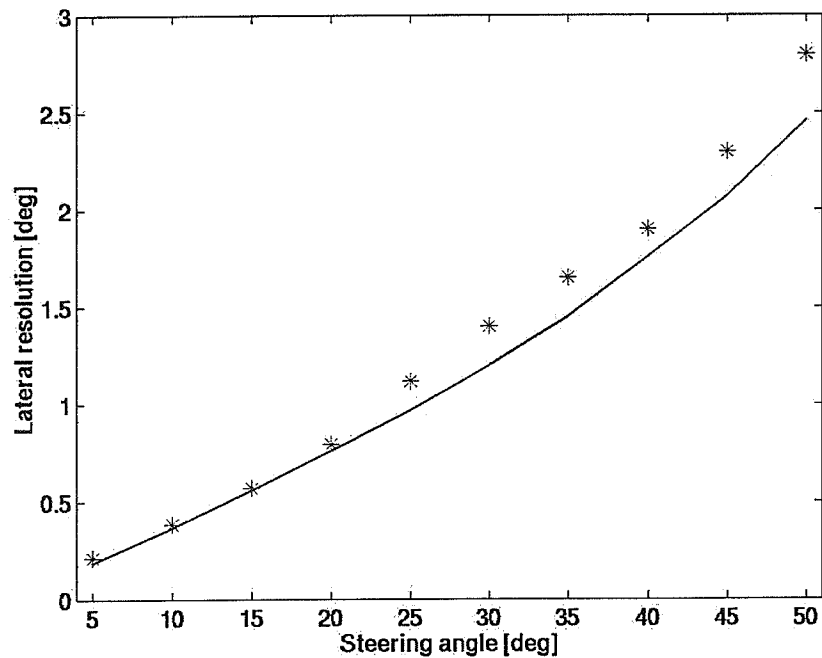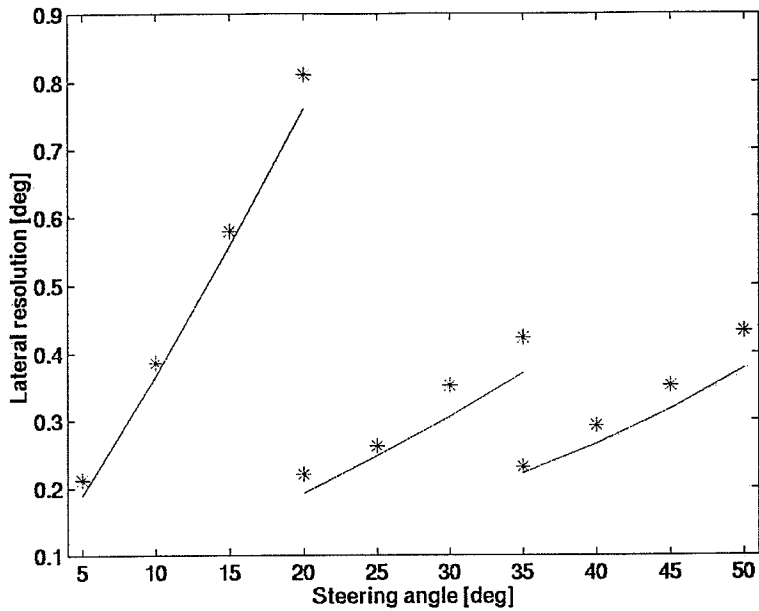Figure 3.27 Variation of the lateral resolution with the steering for a multiple array composed by three arrays designed to steer the beam at respectively 5°, 20°, and 25° for a frequency of 5.6 MHz. The theoretical results are represented by the straight line, the experimental results are represented by the '*'.

Figure 3.28 Spectrogram of four point targets for multiple arrays. The targets have the same range of 2 m and their polar coordinates are respectively 10°, 18°, 35°, and 57°. The three arrays are designed to steer at respectively 5°, 22°, 35°, and 50° for the same frequency of 5.6 MHz.
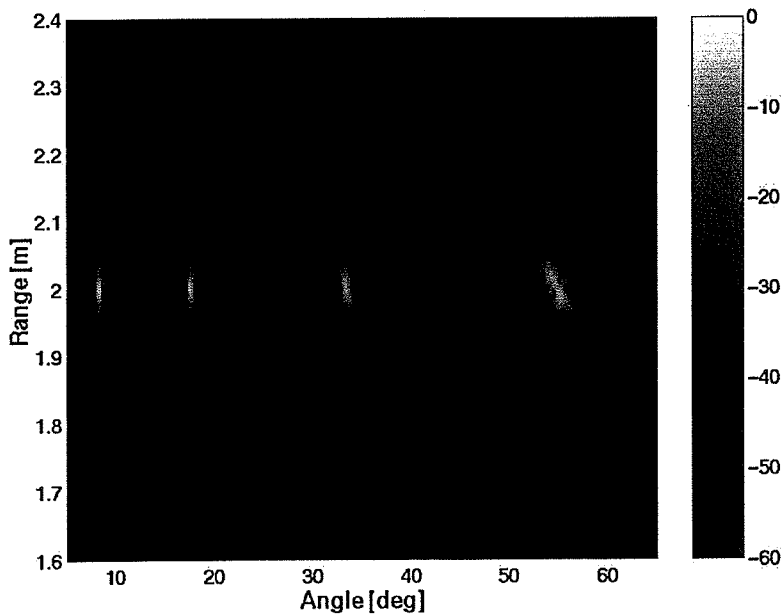
CHAPTER 4

CONCLUSION

4.1. Summary of the Results

The amplitude-steered array is an efficient real-time imaging system: its frame rate is higher than the frame rate of conventional imaging and the electronics used to steer the beam have less complexity. Conventional methods of data collection require at least one pulse per line in the image; thus, the depth of field is limited, unless the frame rate or the quality of the image is sacrificed. The amplitude-steered array images the entire field of view for each pulse transmitted; thus, the number of images obtained per second is higher. For this array, the determination of the angular position of the objects in the field of view depends on the frequency of the emitted signal. This property is unique to the amplitude-steered array and yields interesting trade-offs.

- Steering angle

Axial and lateral resolutions are better for the sector near the normal of the array than for the sector far from the axis.

- Length of the array

There is a trade-off between axial and lateral resolutions related to the length of the array. It was shown that targets separated only in range could be distinguished because frequencies were not separated perfectly, but rather overlapped, As a result, axial resolution improves when the beam width increases, whereas lateral resolution gets worse. The width of the beam at each frequency decreases as the array length increases; therefore, large arrays yield poor axial resolution and good lateral resolution.

- Range of the objects

Where the field of view is in the near field, the effects of the side lobes cannot be neglected. Therefore, the beams overlap more and this yields a trade-off between axial and

76

lateral resolution: the axial resolution improves in the far field, as opposed to the lateral resolution. It has been determined that the amplitude-steered array can be used to image objects whose range is equal or greater than 20 cm. To image a field of view below 20 cm, further processing is needed.

- Effects of the attenuation

The fact that the beam steering depends on the frequency of the signal also gives interesting results in an attenuating medium. In the human body, for example, the attenuation increases with frequency. Since the beam gets closer to the axis of the array when the frequency increases, the signals representing the sector near the axis are the most attenuated, and the image has a lower signal-to-noise in that region than in the rest of the image. This could cause an object to disappear if the attenuation in the medium is large or if the object is far from the array.

- Broadening of the angular sector

The angular sector swept by the beam depends on several factors. First, each array is designed to steer the beam to a particular angle, called the design angle, at a particular frequency, called the design frequency. Second, the frequency in the signal varies and the range of frequencies used determines the width of the angular sector swept by the beam. The design angle, the design frequency, and the range of frequencies determine the field of view. If a single array is excited, the performance of the array is acceptable for an angular sector of 20°. This sector can be extended to 40° by increasing the frequency, but the quality of the image may be degraded by the presence of grating lobes. To overcome this problem, several arrays with different design angles and design frequencies can be excited successively. The sector swept by the beam is broadened and the image has a high quality throughout the entire field of view.

4.2. Future Work

4.2.1. Dimensionality of the problem

The system studied in this thesis is two-dimensional. However, because of the need of three-dimensional imaging in medical applications, several real-time three-dimensional systems have been developed. For example, researchers from Duke University have a real-time volumetric imaging system that is currently in operation [Smith et al., 1991]. But the images are not high quality and the frame rate is only 8 frames per second. In her Ph.D. dissertation, *Frazier*

studies a three-dimensional system using an amplitude-steered array in one dimension and a linear phased array in the other dimension [2000a]. The results look promising, and the possibility of developing a full two-dimensional amplitude-steered array is discussed. Most likely, amplitude-steering would have to be combined with pulse coding to realize such a system.

4.2.2. Nonlinear propagation

Because the angular position is determined by the frequency of the received signal, the amplitude-steered array does not need to transmit multiple pulses to insonify the entire field of view, which yields a fast image formation. However, sound propagation in water and other media is nonlinear, so that harmonics of the transmitted signal are generated as the wave propagates. The frequencies generated could be considered additional targets close to the array broadside direction. Nonlinearity for the amplitude-steered array has not been taken into account in this study, but it could be an interesting problem to study.

4.2.3. Phase aberration

In this thesis, the assumption that the speed of sound is constant in the medium of propagation has been made. However, in the body, different tissues have different speeds of sound ranging from 1450 m/s for fat to 1580 m/s for liver [*Shung*, 1992]. This variability gives rise to a phase aberration problem. The focusing of the beam is calculated on geometrics concerns, so that the pulses from all the elements arrive at a point at the same time. If the speed along the different paths is different, the actual delays contain some perturbation and yield phase aberration. A fair amount of research has been done to solve this problem [*Trahey*, 1989], [*Karaman et al.*, 1991]. However, no good compromise between quality of correction and complexity has yet been found.

4.2.4. Nondestructive evaluation and subsurface imaging

Initially, the amplitude-steered array was developed for underwater applications. This thesis focuses on the use of this array in medical imaging, and the experiments simulate the propagation in human tissues. However, other applications, such as nondestructive evaluation and subsurface imaging, can also potentially benefit from this work.

REFERENCES

Berne, R. B.,*Physiology,* 4th ed., Mosby, St. Louis, 1998.

Frazier, C. H., et al., Analysis of the resolution for an amplitude-steered array, *J. Acoust. Soc. Am.,107* (5), 2430-2436, 2000.

Frazier, C. H., A two-dimensional amplitude-steered array for real-time volumetric acoustic imaging, Ph.D. dissertation, University of Illinois, Urbana-Champaign, 2000.

Fujii, M., et al., Study of the cause of the temperature rise at the muscle-bone interface during ultrasound hyperthermia, *IEEE Trans Biomed Eng, 46 (5),* 494-504, 1999.

Hedrick, W. R., et al., *Ultrasound Physics and Instrumentation,* Mosby-Year Book, 1995.

Hughes, W. J., and P. Thomas, *American Genesis: A Century of Invention and Technological Enthusiasm, 1870-1970,* New York: The Viking Press, 1989.

Hughes, W. J., et al., Transducer Array Scanning System, U. S. Patent 3,905,009, September 9, 1975.

Hughes, W. J., and W. Thompson, Tilted directional response patterns formed by amplitude weighting and a single 90° phase shift, *J. Acoust. Soc. Am., 59* (5), 1040-1045, 1976.

Jensen, J. A., *Estimation of the Blood Velocities Using Ultrasound: A Signal Processing Approach,* Cambridge University Press, 1996.

Jensen, J. A., Field: A program for simulating ultrasound systems, *Med. Biol. Engr. Comp., 34* (1), 351-353, 1996.

Kanai H., et al., A new method for measuring small local vibrations in the heart using ultrasound, *IEEE Trans. Biomed. Eng., 40* (12), 1233-42, 1993.

Karaman, M., et al., Adaptive digital beamforming for phased array ultrasound imaging, *1991 Ultrasonics Symposium,* 2, 1207-1210, 1991.

Kelves, B. H., *Naked to the Bone: Medical Imaging in the Twentieth Century,* pp. 4-10, New Brunswick, N. J.: Rutgers University Press, 1997.

Kinsler, L. E., et al., *Fundamentals of Acoustics,* 4th ed., John Wiley & Sons, New York, 2000.

LaFollette, P. S. Jr., and M. C. Ziskin, Geometric and intensity distortion in echography, *Ultrasound Med. Biol., 12* (12), 953-963, 1986.

Passmann, C., and H. Ermert, A 100-MHz ultrasound imaging system for dermatologic and ophthalmologic diagnostics, *IEEE Trans UFFC, 43* (4), 545-552, 1996.

Porder, J. B., Ultrasound bioeffects, *Echocardiography, 4* (2), 1987.

Shung, K. K., et al., *Principles of Medical Imaging*, Academic Press, Inc., San Diego, 1992.

Smith, S. W., et al., High-speed ultrasound volumetric imaging system – Part I: Transducer design and beam steering, *IEEE Trans. Ultrason. Ferroelect. Freq. Cont., 38*, 100-108, 1991.

Stephanishen, P. R., Pulsed transmit/receive response of ultrasonic piezoelectric transducers, *J. Acoust. Soc. Am.,69*, 1815-1827, 1981.

Trahey, G. E., Phase aberration measurement and correction in medical ultrasound, *IEEE Engineering in Medicine and Biology Society 11th Annual International Conference, 1*, 397-399, 1989

Tupholme, G. E., Generation of acoustic pulses by baffled plane pistons, *Mathematika, 16*, 209-224, 1969.

Ye, S. G., et al., Ultrasound characterization of normal ocular tissue in the frequency range from 50 MHz to 100 MHz, *IEEE Trans. Ultrason., Ferroelect., Freq. Cont., 42* (1), 8-14, 1995.

Zara, J. M., et al., Intracardiac ultrasound scanner using a micromachine (MEMS) actuator, *IEEE Trans UFFC, 47* (4), 984-993, 2000.